



Title	Storm-Track Response to SST Fronts in the Northwestern Pacific Region in an AGCM
Author(s)	Kuwano-Yoshida, Akira; Minobe, Shoshiro
Citation	Journal of Climate, 30(3), 1081-1102 https://doi.org/10.1175/JCLI-D-16-0331.1
Issue Date	2017-02-01
Doc URL	http://hdl.handle.net/2115/66936
Rights	© Copyright 2017 American Meteorological Society (AMS). Permission to use figures, tables, and brief excerpts from this work in scientific and educational works is hereby granted provided that the source is acknowledged. Any use of material in this work that is determined to be "fair use" under Section 107 of the U.S. Copyright Act September 2010 Page 2 or that satisfies the conditions specified in Section 108 of the U.S. Copyright Act (17 USC § 108, as revised by P.L. 94-553) does not require the AMS' s permission. Republication, systematic reproduction, posting in electronic form, such as on a web site or in a searchable database, or other uses of this material, except as exempted by the above statement, requires written permission or a license from the AMS. Additional details are provided in the AMS Copyright Policy, available on the AMS Web site located at (https://www.ametsoc.org/) or from the AMS at 617-227-2425 or copyrights@ametsoc.org .
Type	article
File Information	JC30 1081-1102.pdf



[Instructions for use](#)



Storm-Track Response to SST Fronts in the Northwestern Pacific Region in an AGCM

AKIRA KUWANO-YOSHIDA

Application Laboratory, Japan Agency for Marine-Earth Science and Technology, Yokohama, Japan

SHOSHIRO MINOBE

Department of Natural History Sciences, Graduate School of Science, and Department of Earth and Planetary Sciences, Faculty of Science, Hokkaido University, Sapporo, Japan

(Manuscript received 22 April 2016, in final form 26 August 2016)

ABSTRACT

The storm-track response to sea surface temperature (SST) fronts in the northwestern Pacific region is investigated using an atmospheric general circulation model with a 50-km horizontal resolution. The following two experiments are conducted: one with 0.25° daily SST data (CNTL) and the other with smoothed SSTs over an area covering SST fronts associated with the Kuroshio, the Kuroshio Extension, the Oyashio, and the subpolar front (SMTHK). The storm track estimated from the local deepening rate of surface pressure (LDR) exhibits a prominent peak in this region in CNTL in January, whereas the storm-track peak weakens and moves eastward in SMTHK. Storm-track differences between CNTL and SMTHK are only found in explosive deepening events with LDR larger than 1 hPa h^{-1} . A diagnostic equation of LDR suggests that latent heat release associated with large-scale condensation contributes to the storm-track enhancement. The SST fronts also affect the large-scale atmospheric circulation over the northeastern Pacific Ocean. The jet stream in the upper troposphere tends to meander northward, which is associated with positive sea level pressure (SLP) anomalies in CNTL, whereas the jet stream flows zonally in SMTHK. A composite analysis for the northwestern Pacific SLP anomaly suggests that frequent explosive cyclone development in the northwestern Pacific in CNTL causes downstream positive SLP anomalies over the Gulf of Alaska. Cyclones in SMTHK developing over the northeastern Pacific enhance the moisture flux along the west coast of North America, increasing precipitation in that region.

1. Introduction

The relationship between the storm track and sea surface temperature (SST) fronts associated with western boundary ocean currents, such as the Kuroshio, the Kuroshio Extension, the Oyashio, and the subpolar front in the northwestern Pacific (NWP) as well as the Gulf Stream in the northwestern Atlantic, has been investigated by analyzing observations, reanalysis data, and sensitivity experiments using global and regional atmospheric models in both ideal and realistic situations (Nakamura et al. 2004; Minobe et al. 2008; Taguchi et al.

2009; Sampe et al. 2010; Kuwano-Yoshida et al. 2010b; Frankignoul et al. 2011; Booth et al. 2012; Ogawa et al. 2012; Taguchi et al. 2012; Iizuka et al. 2013; Kuwano-Yoshida et al. 2013; Small et al. 2014; Smirnov et al. 2015; O'Reilly and Czaja 2015; O'Reilly et al. 2016; Ma et al. 2015; Parfitt et al. 2016). Nakamura et al. (2004) summarized the relationship among storm tracks, jet streams, and midlatitude oceanic fronts based on observations and reanalyses. They found that storm-track activity strengthens within a polar front jet along a near-surface baroclinic zone associated with SST fronts in the Southern Hemisphere or the North Atlantic during the cold season.

A series of aquaplanet experiments using an atmospheric general circulation model (AGCM) has been used to examine the atmospheric response mechanism to zonally uniform SST fronts (Sampe et al. 2010; Ogawa et al. 2012). Sampe et al. (2010) suggested that the SST front anchors a subpolar storm track aloft, leading to a separation of this

 Denotes Open Access content.

Corresponding author e-mail: Akira Kuwano-Yoshida, akiray@jamstec.go.jp

DOI: 10.1175/JCLI-D-16-0331.1

storm track from another storm track associated with a subtropical jet in winter. [Ogawa et al. \(2012\)](#) suggested that a low-level storm track organizes along the SST front if it exists in the subtropics or midlatitudes.

The storm-track response located immediately above SST fronts has been investigated using land-included regional and global models. [Taguchi et al. \(2009\)](#) investigated the atmospheric response over the Kuroshio and Oyashio Extensions (KOE) using a regional atmospheric model. They suggested that the storm-track response is different between winter and spring. In spring, the surface heat flux gradient is prominent over the SST front, resulting in enhanced storm-track activity, although in winter, the cold and dry air advection associated with the Asian winter monsoon induces large heat fluxes on both the cold and warm sides of the SST front, resulting in a weaker atmospheric response to the SST front. [Small et al. \(2014\)](#) investigated the atmospheric response to SST fronts over the Atlantic and south Indian Oceans using 50-km-resolution AGCM experiments with and without SST smoothing. [Small et al. \(2014\)](#) showed that the storm track weakens with the SST smoothing by 10%–20%, and the influence is larger in the boundary layer than in the free troposphere.

Large-scale or remote responses to SST fronts have been argued. [Frankignoul et al. \(2011\)](#) suggested that the KOE meridional shift influences the barotropic atmospheric response over the North Pacific with a 2-month lag when excluding ENSO using observations. Moreover, [Taguchi et al. \(2012\)](#) suggested that the atmospheric response over the North Pacific is limited in January. [O'Reilly and Czaja \(2015\)](#) analyzed the observed storm-track response to the Kuroshio Extension strength, suggesting that the zonal shift in the storm-track peak associated with the SST front modifies the blocking frequency in the northeastern Pacific (NEP). Recently, [O'Reilly et al. \(2016\)](#) showed that the SST front associated with the Gulf Stream modulates wintertime European blocking through storm-track enhancement.

The SST front regions are also the places where explosive extratropical cyclones, so-called bomb cyclones, frequently develop. [Sanders and Gyakum \(1980\)](#) first suggested the relationship between the geographical distribution of explosive cyclones and SST fronts. [Yoshiike and Kawamura \(2009\)](#) found that explosive cyclones are concentrated over the SST front near Japan. [Iizuka et al. \(2013\)](#) showed that explosive cyclones are more concentrated over a sharp SST front than over a smoothed SST front based on regional model experiments. [Iizuka et al. \(2013\)](#) also suggested that the concentration of explosive cyclones over the SST front strengthens under strong monsoon conditions associated with strong horizontal gradients in the equivalent potential temperature in the lower troposphere,

despite the fact that the Eady growth rate in the observed SST experiment did not show a significant difference over the NWP from the smoothed SST experiment. This finding contradicts the results over the Gulf Stream in [Small et al. \(2014\)](#), who showed that the Eady growth rate associated with the Gulf Stream significantly decreases in the smoothed SST front experiment compared with the observed SST front experiment using an AGCM. Furthermore, [Booth et al. \(2012\)](#) showed that an extratropical cyclone is more sensitive to the absolute value of the SST than the SST gradient across the Gulf Stream.

The purpose of the present paper is to understand storm-track and large-scale responses to SST fronts in the NWP using the following two 20-yr integrations of an AGCM with approximately 50-km horizontal resolution: one with observed SST data and the other with smoothed SSTs over the NWP. The remainder of the present paper is organized as follows. The detailed configuration of the model experiments and analysis methods are described in [section 2](#). In [section 3](#), the storm-track response is shown, which is closely related to the zonal shift of explosive cyclone activity. The large-scale responses associated with the zonal shift are described in [section 4](#). The mechanism of the local and large-scale responses is analyzed using composite analyses in [section 5](#), and the intraseasonal dependency is discussed in [section 6](#). Finally, the conclusions are presented in [section 7](#).

2. Model experiment configuration and methods

We use the AGCM for the Earth Simulator (AFES), version 3 ([Ohfuchi et al. 2004](#); [Enomoto et al. 2008](#); [Kuwano-Yoshida et al. 2010a](#)), which has been developed by the Earth Simulator Center and Application Laboratory of the Japan Agency for Marine-Earth Science and Technology (JAMSTEC). The horizontal resolution is spectral T239, corresponding to an approximately 50-km interval, with 48 sigma levels in the vertical from the surface to approximately 3 hPa. NOAA 0.25° daily SST data ([Reynolds et al. 2007](#)) are used for the bottom boundary conditions. The following two experiments are conducted: the control experiment (CNTL) that uses the original NOAA SSTs, and a second experiment (SMTHK) that uses the smoothed SSTs over the NWP (25°–55°N, 120°E–180°) by applying a 1–2–1 running mean filter 200 times in both the zonal and meridional directions on a 0.5° grid ([Fig. 1](#)). In both experiments, the AGCM is integrated for 20 years from 1 September 1981 to 31 August 2001 and is initialized with the Japanese 25-year Reanalysis Project (JRA-25; [Onogi et al. 2007](#)). The time interval of the model output is 6 h.

To investigate the storm-track activity, we use the local deepening rate (LDR), a Eulerian measure of the storm

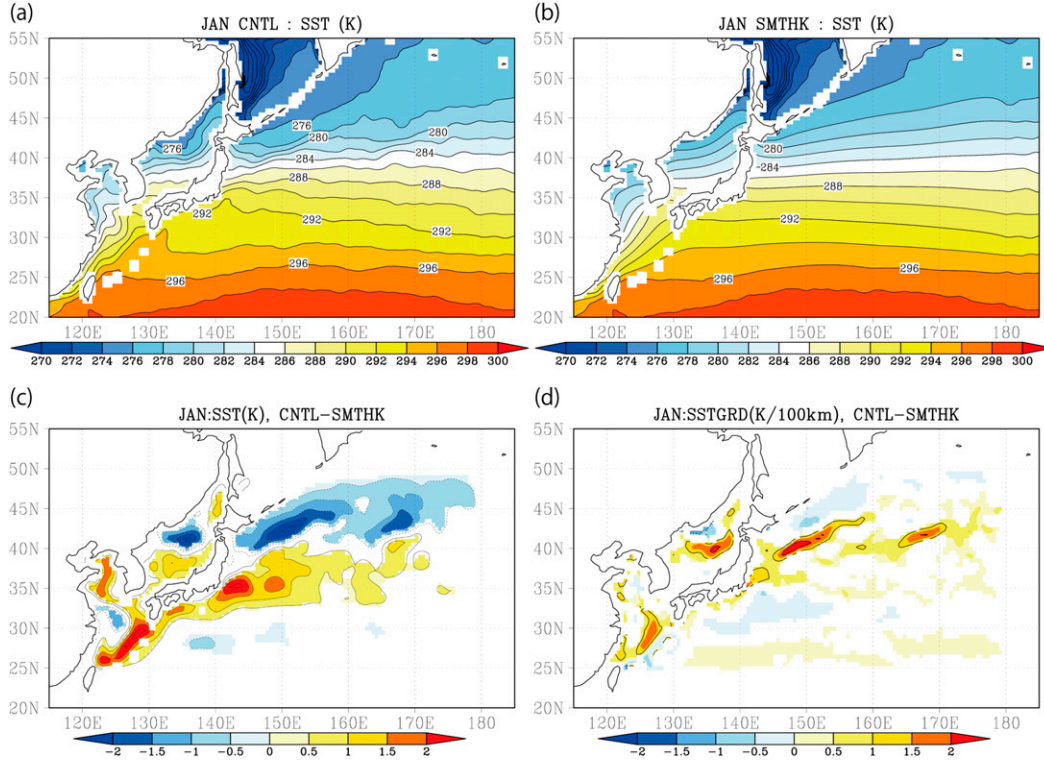


FIG. 1. Climatological SSTs in January for (a) CNTL and (b) SMTHK and (c) the difference between CNTL and SMTHK (K). (d) The difference in the horizontal SST gradient between CNTL and SMTHK [$\text{K} (100 \text{ km})^{-1}$].

track, proposed by [Kuwano-Yoshida \(2014\)](#), which can be defined as follows:

$$\text{LDR} = -\frac{\partial p_{\text{sfc}}}{\partial t} \left| \frac{\sin 60^\circ}{\sin \theta} \right|, \quad (1)$$

where p_{sfc} is the surface pressure, t is the time, and θ is the latitude. In the present study, the 24-h center difference of the surface pressure, which is referred to as LDR24, is computed as follows:

$$\text{LDR24} = -\frac{p_{\text{sfc}}(t+12\text{h}) - p_{\text{sfc}}(t-12\text{h})}{24} \left| \frac{\sin 60^\circ}{\sin \theta} \right|, \quad (2)$$

using 6-hourly surface pressure data. Monthly storm-track activity is estimated using the monthly means of the positive LDR24 (LDR24P0) for all cyclones and $\text{LDR24} \geq 1 \text{ hPa h}^{-1}$ (LDR24P1) for explosive cyclones. As shown in [Kuwano-Yoshida \(2014\)](#), the threshold of

LDR24P1 is equivalent to explosive cyclones defined by the normalized deepening rate based on the cyclone center SLP proposed by [Sanders and Gyakum \(1980\)](#). The LDR24P0 and LDR24P1 are defined as follows:

$$\text{LDR24Pm} = \frac{1}{n} \sum_{i=1}^n \sigma_m(t=i),$$

$$\sigma_m = \begin{cases} \text{LDR24}, & \text{if } \text{LDR24} \geq m \text{ hPa h}^{-1} \\ 0, & \text{otherwise} \end{cases}, \quad (3)$$

where n is the number of time steps in the month, and m is a threshold (0 or 1 hPa h^{-1}). Note that LDR24P0 is the sum of LDR24P1 and the sum of LDR24 between 0 and 1 hPa h^{-1} divided by n .

One of the advantages of the LDR is that the factors influencing it can be diagnosed using the pressure tendency equation introduced by [Fink et al. \(2012\)](#):

$$\text{LDR} = -\frac{\sin 60^\circ}{\sin \theta} \left[\rho_{\text{sfc}} \frac{\partial \phi_{p_2}}{\partial t} + \rho_{\text{sfc}} R_d \int_{\text{sfc}}^{p_2} \frac{\partial T_v}{\partial t} d \ln p + g(E - P) + \text{RES}_{\text{PTE}} \right], \quad (4)$$

where p is the pressure, ρ_{sfc} is the surface air density, ϕ_{p_2} is the geopotential height at p_2 (100 hPa), R_d is the gas constant for dry air, T_v is the virtual temperature, g is the gravity acceleration, E is the surface evaporation, P is the surface precipitation, and RES_{PTE} is the residuum due to discretization. The first term represents the contribution of the geopotential tendency above the troposphere (referred to as $D\phi$), the second term is the vertically integrated virtual temperature tendency (ITT), and the third term is the moisture mass budget (EP). The ITT can be expanded as follows:

$$\begin{aligned} \text{ITT} &= \rho_{\text{sfc}} R_d \int_{\text{sfc}}^{p_2} -\mathbf{v} \cdot \nabla_p T_v d \ln p \quad (\text{HADV}) \\ &+ \rho_{\text{sfc}} R_d \int_{\text{sfc}}^{p_2} \left(\frac{R_d T_v}{c_p p} - \frac{\partial T_v}{\partial p} \right) \omega d \ln p \quad (\text{VADV}) \\ &+ \rho_{\text{sfc}} R_d \int_{\text{sfc}}^{p_2} \frac{T_v Q}{c_p T} d \ln p \quad (\text{DIAB}) \\ &+ \text{RES}_{\text{ITT}}, \end{aligned} \quad (5)$$

where \mathbf{v} is the horizontal velocity vector, ω is the vertical pressure velocity, T is the temperature, c_p is the specific heat capacity, Q is the diabatic heating rate, and RES_{ITT} is the residuum due to discretization. The first term on the right-hand side indicates horizontal temperature advection (HADV), the second term represents vertical advection (VADV), and the third term is diabatic heating (DIAB). In the present study, the ITT terms are calculated from 24-h averages of 6-hourly temperature and moisture tendency outputs from the dynamical and physical processes of the AFES. The sum of HADV and VADV gives the dynamic tendency (DYN). DIAB is further expanded into the components due to large-scale (grid scale) condensation (LSC), cumulus convection (CUM), vertical diffusion (VDF), shortwave radiation (RADS), and longwave radiation (RADL).

Other parameters widely used for storm-track analysis are also analyzed. The Eady growth rate (EGR; Lindzen and Farrell 1980) is given by

$$\text{EGR} = 0.31 \frac{f}{N} \left| \frac{d\mathbf{v}}{dZ} \right|, \quad (6)$$

where f is the Coriolis parameter, N is the Brunt–Väisälä frequency, and Z is the geopotential height. In this study, the EGR is estimated at 850 hPa using monthly mean values at 925 and 775 hPa for stability and vertical wind shear. In addition, eddy components of the meridional heat flux $v'T'$, moisture flux $v'q'$ and meridional wind variance $v'v'$ are used as other measures of the storm track, where the prime indicates that a high-pass filter is used to extract variations shorter than 8 days.

The statistical significance of the monthly climatological mean difference between the CNTL and SMTHK simulations is calculated using Monte Carlo resampling. Two sets of 20-yr data are made by shuffling the CNTL and SMTHK output for each month; the difference is saved. This process is repeated 2000 times to assess the probability that the difference between the datasets could occur by chance. The significance of the composite analysis for explosive deepening events against slow deepening events in section 5 is estimated using a Student's t test.

3. Storm-track response

First, we analyze the storm-track response to NWP SST fronts using the monthly LDR24P0 climatology in CNTL and SMTHK for December, January, and February (Figs. 2a,c,e). The storm-track response expressed as the difference in LDR24P0 between CNTL and SMTHK over the NWP is the most significant and well organized in January; in December, nearly no statistically significant difference occurs, and in February, significant changes are zonally distributed over wider areas without well-organized patterns. This intraseasonal dependency is also apparent in LDR24P1 (Figs. 2b,d,f). Therefore, we focus our attention on the January response in the present study. The LDR24P0 difference in January shows that LDR24P0 in CNTL is larger over the NWP and smaller over the NEP than that in SMTHK (Fig. 2c). The LDR24P1 difference primarily explains this LDR24P0 response (Fig. 2d). The meridionally averaged LDR24P1 between 30° and 50°N exhibits a strong peak over NWP in CNTL, whereas in SMTHK, the maximum LDR24P1 is reduced and shifts eastward owing to a zonally flatter LDR24P1 distribution (Fig. 3a). The PDF of LDR24 over the NWP shows that the frequency of $\text{LDR24} > 1$ in CNTL increases and the frequency of $0 < \text{LDR24} < 1$ in CNTL decreases compared to SMTHK (Figs. 3b,c). The weighted PDF, in which frequency multiplied by LDR24 is integrated for each 0.1 bin, shows that a large difference appears when LDR24 exceeds 1 hPa h^{-1} (Figs. 3d,e). This means that LDR24P1 largely explains the LDR24P0 difference shown in Fig. 2c because the area of the weighted PDF exceeding 1 hPa h^{-1} divided by the number of time steps in the month is LDR24P1. The results reveal that the NWP SST front acts to increase explosive deepening events in extratropical cyclones, consistent with Iizuka et al. (2013), who reported that explosive cyclones are concentrated over the NWP SST front using an SST smoothing experiment in a regional model. With the smoothed SST front, the frequency of explosive deepening events increases over the NEP, and this feature is

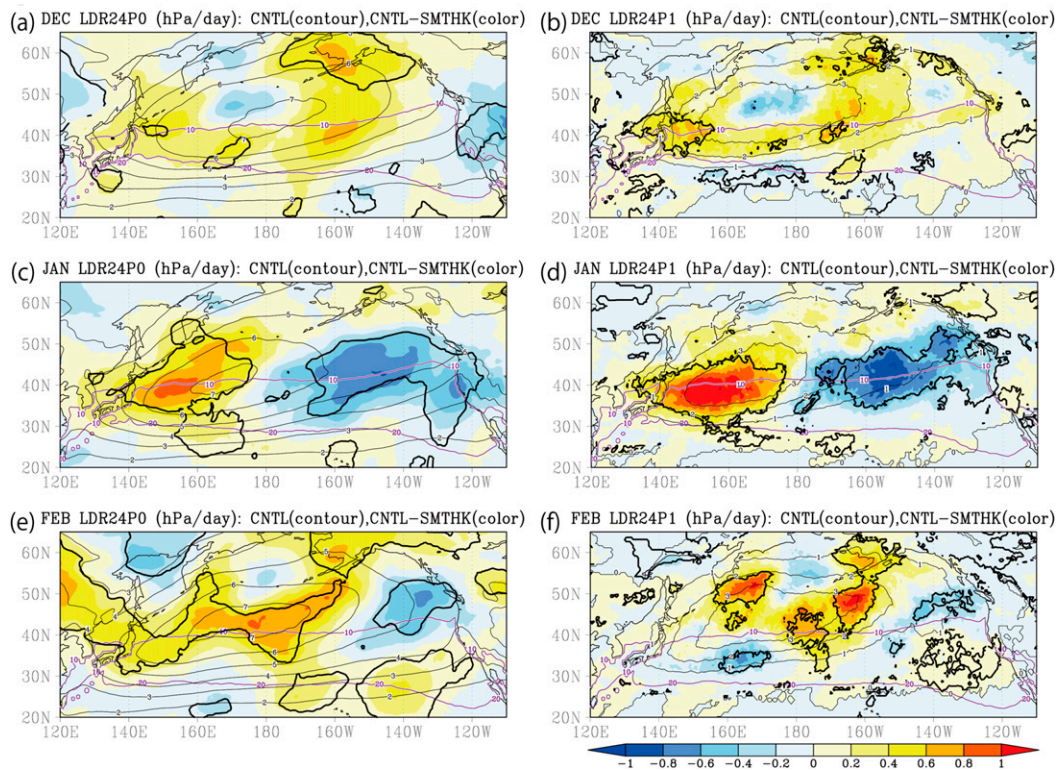


FIG. 2. (left) LDR24P0 and (right) LDR24P1 (thin black contours; hPa day^{-1}) in CNTL and the difference between CNTL and SMTHK (shaded) in (a),(b) December, (c),(d) January, and (e),(f) February. The 95% confidence level is shown by thick black contours. The purple contours show SSTs at 10° and 20°C .

similar to the storm-track response to Kuroshio Extension variability in O'Reilly and Czaja (2015).

Conventionally used storm-track indices, such as the EGR, $v'T'$, and $v'v'$ (Nakamura and Yamane 2010; Sampe et al. 2010; Woollings et al. 2010; Hotta and Nakamura 2011; Ogawa et al. 2012; Iizuka et al. 2013; Small et al. 2014), are also examined. Figure 4a shows the EGR difference at 850 hPa between CNTL and SMTHK in January (EGRC – EGRS). One might assume that the EGR is generally larger for a sharp SST front than for a smoothed one based on the numerical experiments for the Gulf Stream by Small et al. (2014). However, the significant positive anomaly in the EGR difference at 850 hPa between CNTL and SMTHK is weak and spatially limited over the NWP SST front, sandwiched by wider negative differences to the north and south. The present result is consistent with regional model experiments for the NWP SST front in Iizuka et al. (2013).

The EGR is composed of vertical wind shear and static stability components [Eq. (6)]. To estimate the SST front contribution to the EGR, we calculate the other following two types of EGR: one is EGRSC from static stability in SMTHK and the vertical wind shear in

CNTL, and the other is EGRCS from the static stability in CNTL and the vertical wind shear in SMTHK. The estimation is similar to that used by Yin (2005). The difference between EGRC and EGRCS suggests that over the NWP SST front, vertical wind shear in CNTL contributes positively to the EGR along the SST front (Fig. 4b), although the difference between EGRC and EGRCS shows that static stability in CNTL has a negative contribution, especially north of the SST front (Fig. 4c). The negative contribution of static stability to the EGR along the northern side of the SST front is due to the negative sensible heat flux anomaly associated with the colder SSTs in CNTL than in SMTHK (Figs. 1c and 4e). The negative sensible heat flux anomaly strengthens the static stability in the lower troposphere and reduces the EGR.

The negative static stability contribution also extends east of the Okhotsk Sea, where the negative SST anomaly is small (Fig. 4c). The negative contribution appears along the southern and eastern edges of the positive SLP anomaly region in CNTL (compared to SMTHK) over the Okhotsk Sea (Fig. 4d). The high pressure anomaly enhances cold advection at 925 hPa, crossing over the warm side of the SST front from the

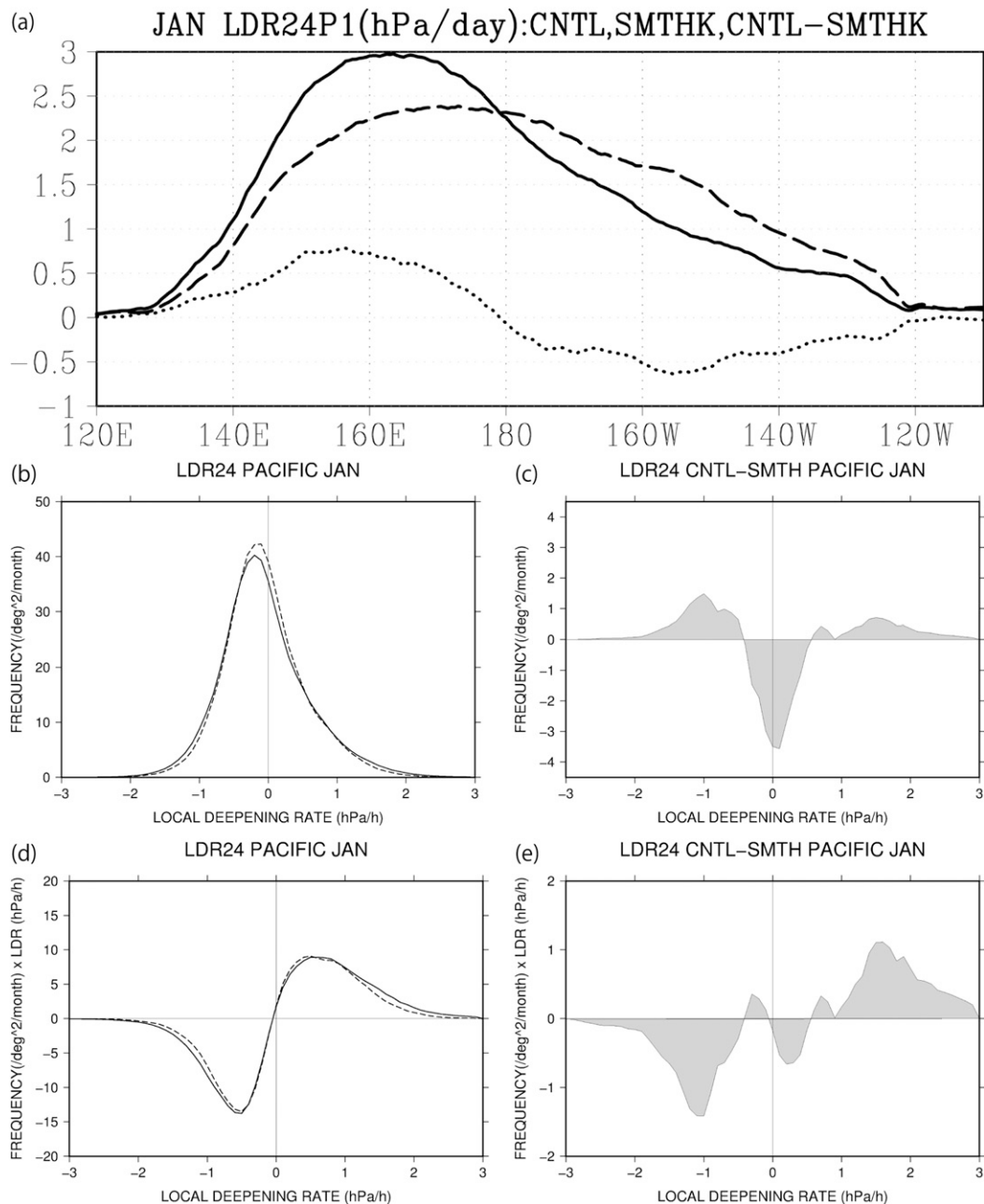


FIG. 3. (a) Meridional average of LDR24P1 (hPa day^{-1}) between 30° and 50°N in CNTL (solid line), SMTHK (dashed line), and the difference between CNTL and SMTHK (dotted line) in January. (b) PDF of LDR24 (hPa h^{-1}) within 140° and 170°E , 30° and 50°N [$(^{\circ}\text{lat/lon})^2 \text{ month}^{-1}$] in CNTL (solid line) and SMTHK (dashed line) and (c) the difference between CNTL and SMTHK. (d),(e) As in (b),(c), but for the weighted PDF (see text).

Siberia high in CNTL (Fig. 4g). The cold advection strengthens the static stability in the lower troposphere in CNTL and offsets the positive impact of the warm SST anomaly on the EGR. Because the magnitude of the negative contribution of the low SSTs is comparable to the positive contribution due to the strong vertical

wind shear associated with the sharp SST front in CNTL, the EGR difference between CNTL and SMTHK over the NWP SST front becomes small.

The different characteristics of the sensible and latent heat fluxes can explain the small change in the EGR contradicting the substantial increase in explosive

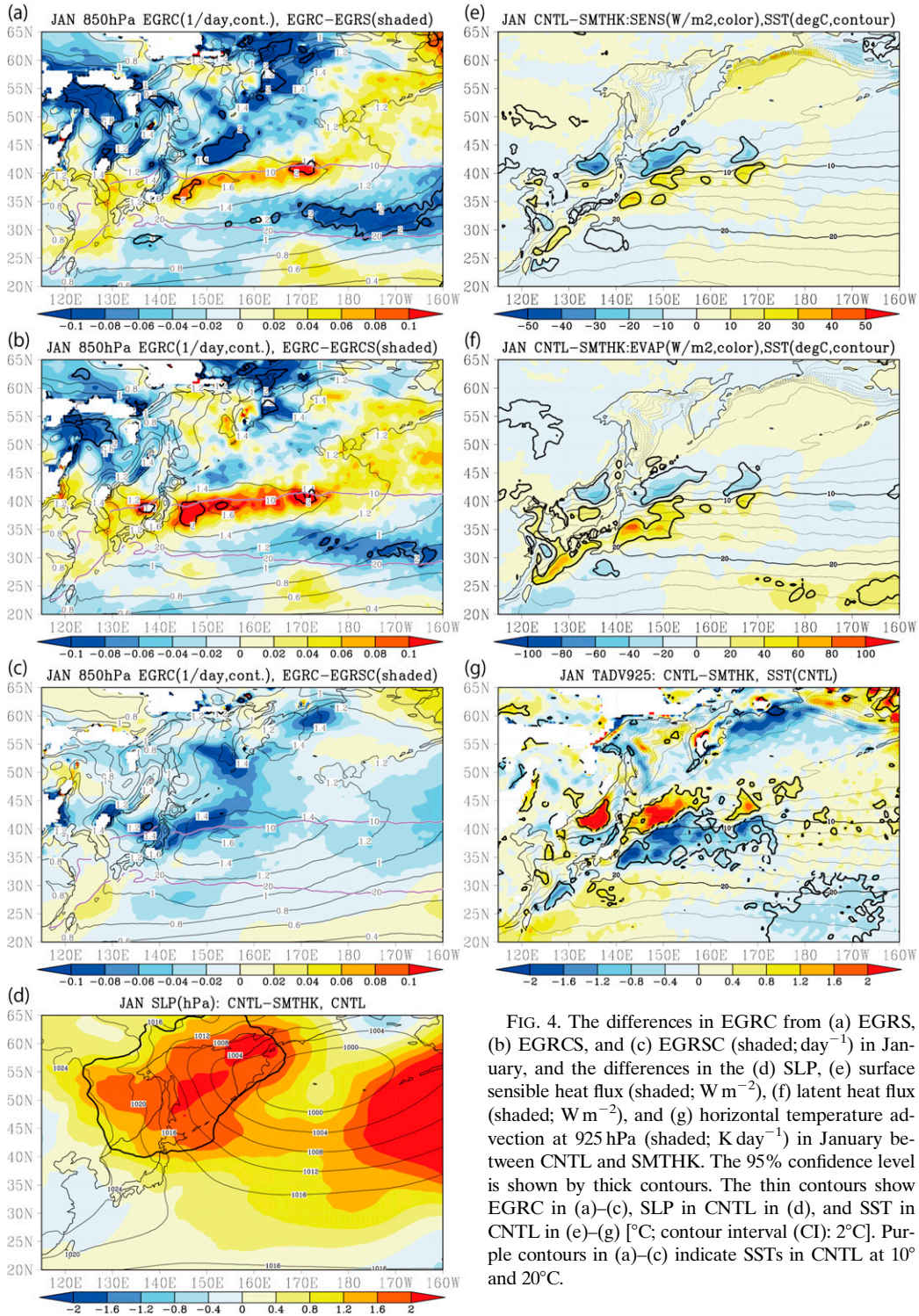


FIG. 4. The differences in EGRC from (a) EGRS, (b) EGRCS, and (c) EGRSC (shaded; day⁻¹) in January, and the differences in the (d) SLP, (e) surface sensible heat flux (shaded; W m⁻²), (f) latent heat flux (shaded; W m⁻²), and (g) horizontal temperature advection at 925 hPa (shaded; K day⁻¹) in January between CNTL and SMTHK. The 95% confidence level is shown by thick contours. The thin contours show EGRC in (a)–(c), SLP in CNTL in (d), and SST in CNTL in (e)–(g) [°C; contour interval (CI): 2°C]. Purple contours in (a)–(c) indicate SSTs in CNTL at 10° and 20°C.

events in CNTL compared with SMTHK. The sensible (latent) heat flux is more significant north (south) of the SST front (Figs. 4e,f), owing to higher background SSTs to the south combined with the Clausius–Clapeyron

relation. The meridionally antisymmetric structure of the surface heat flux results in a different atmospheric response to SST smoothing. The positive anomaly in the latent heat flux (LHF) south of the SST front in CNTL

contributes to the explosive deepening through precipitation (Yoshida and Asuma 2004; Kuwano-Yoshida and Asuma 2008; Hirata et al. 2015). However, the negative anomaly in the sensible heat flux north of the SST front weakens the EGR at approximately 43°N, suppressing cyclone development north of the SST front.

Storm-track strength measured by $v'T'$, $v'v'$, and $v'q'$ shows different responses. The differences in $v'T'$ between CNTL and SMTHK are very small over the NWP SST front, whereas the differences in $v'v'$ and $v'q'$ exhibit zonal dipole patterns similar to that of LDR24P1 (Fig. 5). These results suggest that the increase in explosive deepening events enhances the meridional wind and moisture transport eddy components in CNTL, although the meridional heat transport by the eddy components does not substantially change between CNTL and SMTHK. This finding suggests that moist processes are more important to the explosive deepening in CNTL than dry processes estimated by the EGR and $v'T'$.

To understand how the LDR24P1 response occurs, the LDR is diagnosed using Eqs. (4) and (5). The monthly averages of each term in Eqs. (4) and (5) are computed such that grids where $LDR_{24} \geq 1$ are added and the other grids are added as zero in the average to estimate the contribution to LDR24P1. The differences in the monthly averages between CNTL and SMTHK show that the ITT explains a majority of the LDR24P1 difference (Fig. 6a). The $D\phi$ and EP exhibit only a small contribution to the difference, although the EP difference is statistically significant (Figs. 6b,c). The present results are consistent with Fink et al. (2012), who showed that the ITT is the dominant component of explosive cyclone development over the North Atlantic.

The contributions of dynamical and physical processes to the ITT difference show that the latent heat release of LSC plays a dominant role (Fig. 7). In CNTL, LSC strengthens the ITT, whereas RADL weakens it over the NWP. In SMTHK, LSC contributes to the large LDR24P1 in the NEP. Because the latent heat release associated with condensation is a major developing factor for explosive cyclones over the NWP (Yoshida and Asuma 2004; Kuwano-Yoshida and Asuma 2008), the result suggests that the NWP SST front contributes to explosive cyclone development by changing the latent heat release. The detailed process of latent heat release in the individual cyclone is discussed in section 5.

4. Large-scale response

The monthly mean fields of SLP and geopotential height in January show the large-scale response to the

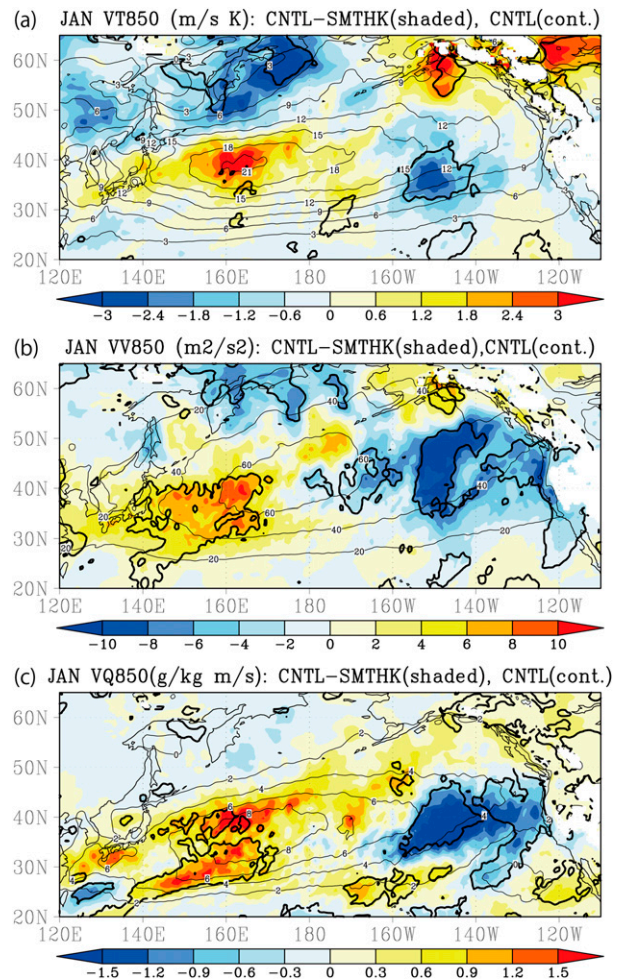


FIG. 5. The differences in (a) $v'T'$ (shaded; $\text{m s}^{-1} \text{K}$), (b) $v'v'$ (shaded; $\text{m}^2 \text{s}^{-2}$), and (c) $v'q'$ ($\text{g kg}^{-1} \text{m s}^{-1}$) at 850 hPa between CNTL and SMTHK in January. The 95% confidence level is shown by thick contours. The means of CNTL are shown by thin contours.

NWP SST front (Fig. 8c). Their positive anomalies in CNTL compared with SMTHK appear barotropically over the Gulf of Alaska from the surface to 500 hPa (Fig. 8d). Although large interannual variability associated with the Aleutian low decreases the confidence level over the central North Pacific, these responses are similar to the atmospheric responses to the interannual and decadal variations of the NWP SST front (O'Reilly and Czaja 2015; Taguchi et al. 2012). The large-scale response in January is larger than that in December and February (Figs. 8a,e), which is consistent with Taguchi et al. (2012).

The large-scale atmospheric response can be understood as the meridional migration of the westerly jet axis in the upper troposphere over the NEP. Figure 9 displays the occurrence frequency of the upper-level jet axis detected by the meridional maximum of the

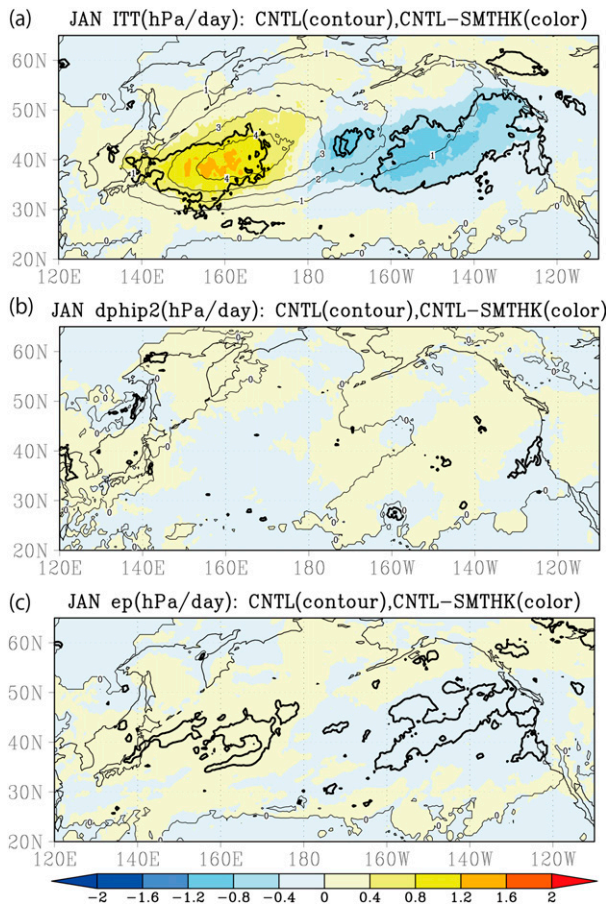


FIG. 6. Monthly average (a) ITT, (b) $D\phi$, and (c) EP in January (hPa day^{-1}) for LDR24P1 in CNTL (contour) and the difference between CNTL and SMTHK (shaded). The 95% confidence level is shown by thick contours.

westerly wind velocity in the Northern Hemisphere at 300 hPa for each longitude using 6-h zonal wind. In CNTL, the frequency of the jet axis spreads meridionally in the NEP with two maxima along 48° and 35°N (Fig. 9a), whereas the jet axis is concentrated around 35°N in SMTHK (Fig. 9b). As a result, the monthly mean zonal wind velocity in CNTL is less than that of SMTHK over the NEP at approximately 35°N by more than 6 m s^{-1} (Fig. 9c). These results, combined with the more frequent explosive cyclones in CNTL shown in the previous section, suggest that the enhanced cyclone development over the NWP SST front causes the upper-level jet fluctuations in the NEP in CNTL.

The jet response affects moisture transport and the precipitation distribution. The westerly horizontal moisture flux in CNTL is weaker than that in SMTHK because of the weaker jet in the NEP; thus, precipitation along the west coast of North America decreases (Fig. 10), whereas precipitation increases southeast of Hawaii. Yoshiike and

Kawamura (2009) suggested that downstream teleconnection of explosive cyclone events over the NWP affects Kona storms, damaging the Hawaiian Islands. The relationship between individual cyclones and the large-scale response is analyzed using composite analyses in the next section.

5. Composite analysis

The results in the previous sections indicate enhanced (weakened) cyclone development over the NWP (NEP) and stronger meandering of the upper-level jet over the NEP in CNTL compared with SMTHK. To understand the explosive deepening mechanism over the NWP SST front and the relationship between the storm-track response and the large-scale responses, lag-composite analyses for explosive deepening events with $\text{LDR24} \geq 1$ and slow deepening events with $0 < \text{LDR24} < 1$ over the NWP in CNTL and SMTHK are conducted. In this analysis, we focus our attention on the relationship between explosive deepening events to precipitation and upper-level disturbances propagating from the west because these factors generally play important roles in explosively developing extratropical cyclones (Shapiro et al. 1999; Yoshida and Asuma 2004). The reference time series for the composite is LDR24 at 39°N , 153°E , corresponding to the maximum LDR24P1 difference (Fig. 2d). For the explosive deepening events, the time when the reference LDR24 exceeds unity for the first time is regarded as lag zero ($T = 0$). For the slow deepening events, the time when the reference LDR24 exceeds zero, which is smaller than unity and has increased over the prior 6 h, is regarded as lag zero. The sample sizes for each event are summarized in Table 1.

Figure 11 shows the lag composite of the NWP explosive deepening events from $T = -12$ to 24 h in CNTL and their differences from SMTHK. The composites clearly show the cyclone structure and its relationship with the SST front. At $T = -12$ h, a weak cyclone appears over the Sea of Japan associated with weak precipitation over western Japan in CNTL and moisture flux into the area from the East China Sea and the Kuroshio (Fig. 11a). Positive precipitation anomalies associated with the cyclone in CNTL overlap the cyclone over the Japan Sea, whereas negative precipitation anomalies are elongated to the south of the Kuroshio and are associated with northerly moisture flux anomalies in the subtropics in CNTL – SMTHK (Fig. 11b). The features reveal that the moisture flowing into the explosive cyclones in SMTHK comes from the subtropics, not the Kuroshio. At $T = 0$ h, the surface LHF over the Kuroshio along the south coast of Japan in

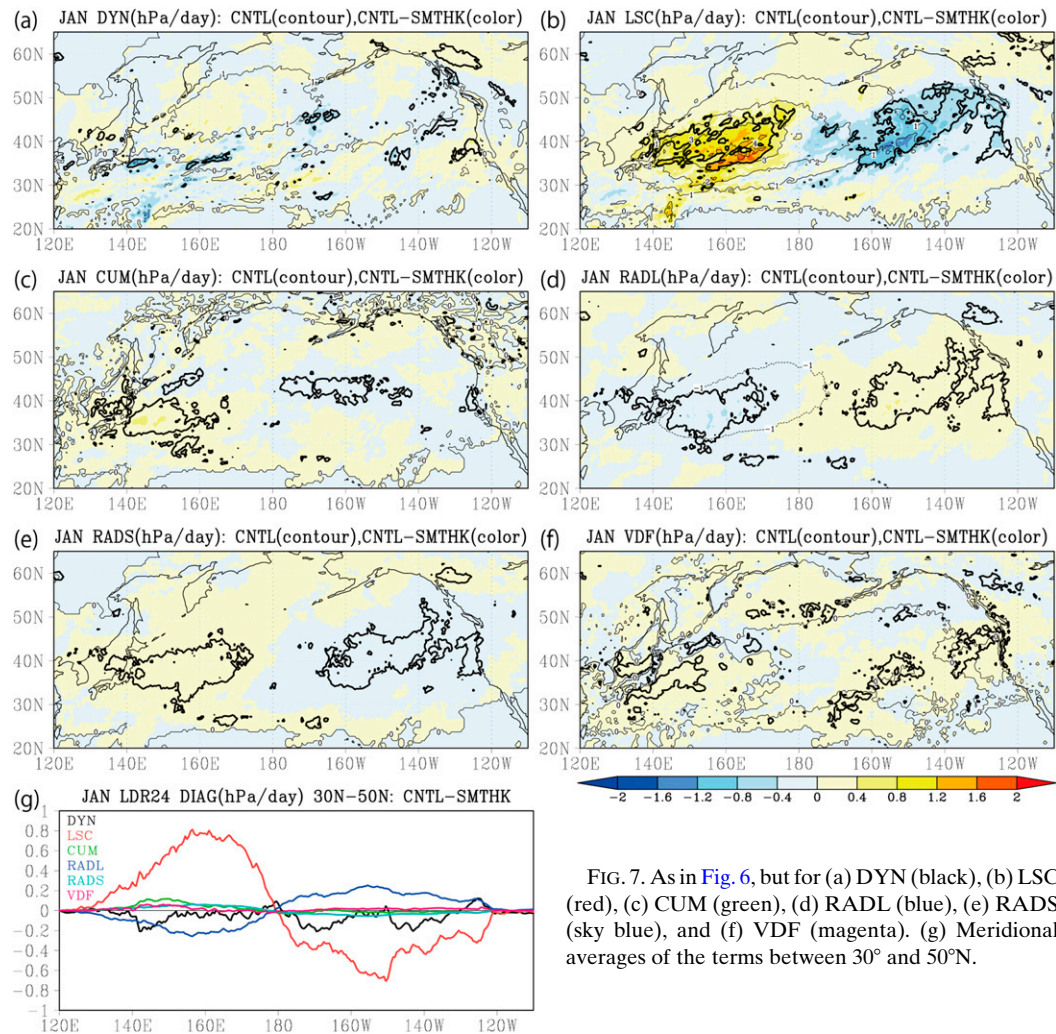


FIG. 7. As in Fig. 6, but for (a) DYN (black), (b) LSC (red), (c) CUM (green), (d) RADL (blue), (e) RADS (sky blue), and (f) VDF (magenta). (g) Meridional averages of the terms between 30° and 50°N.

CNTL is larger than that in SMTHK, and the precipitation difference is concentrated over the Kuroshio according to CNTL – SMTHK (Fig. 11d). Moreover, negative precipitation anomalies appear south of the Kuroshio. This means that the LHF associated with the Kuroshio strengthens precipitation near the cyclone center in CNTL, whereas horizontal moisture flux from the subtropics contributes more to precipitation in SMTHK. At $T = 12$ h, the cyclone moves east of Japan and is accompanied by stronger precipitation overlapping the cyclone center in CNTL (Fig. 11e). The large surface LHF occurs just southwest of the precipitation area, and a negative SLP anomaly develops north of the Kuroshio and its extension (Fig. 11f). These results suggest that the SST front over the NWP enhances precipitation near the cyclone center through the large surface LHF from the Kuroshio and its extension. The precipitation enhancement causes the explosive deepening over the NWP in CNTL, consistent with regional model experiments for

explosive cyclones due to SST fronts (Booth et al. 2012; Iizuka et al. 2013; Hirata et al. 2015).

The precipitation difference between CNTL and SMTHK associated with the explosive deepening also affects the upper troposphere. Figure 12 displays the basin-scale composite differences in the geopotential height at 300 hPa between the explosive and slow deepening events in CNTL and SMTHK. Here, the difference is taken to enhance the characteristics of the explosive deepening events. At $T = -24$ h, the geopotential height anomaly shows a wave train propagating from China to the NWP with weak wave activity fluxes (Takaya and Nakamura 1997) in Fig. 12a. When explosive deepening occurs ($T = 0$ h), the positive geopotential height anomaly is amplified downstream of the surface cyclone (Figs. 11c and 12c). This enhances the westward-tilted geopotential anomaly structure with height. At $T = 24$ h, the upper-level positive geopotential height anomaly amplifies further and becomes the source of the

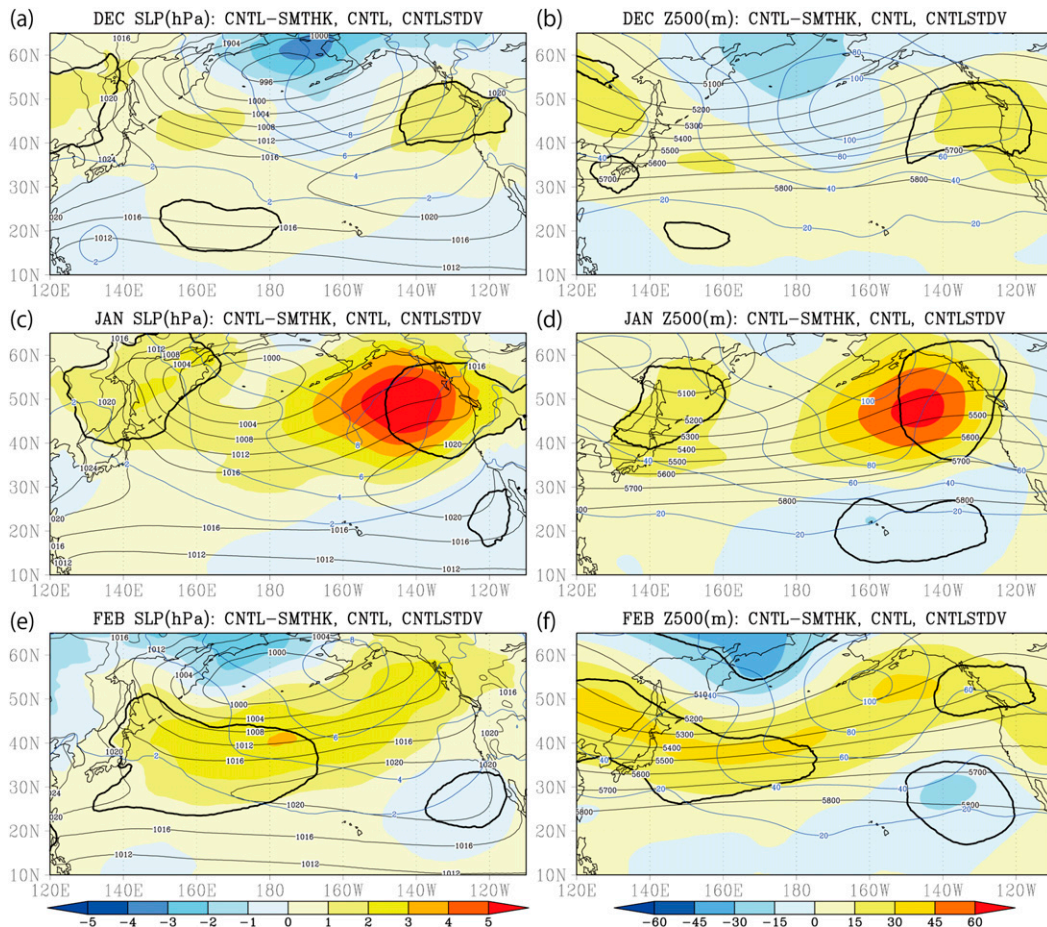


FIG. 8. Monthly average (left) SLP (hPa) and (right) geopotential height at 500 hPa (m) in (a),(b) December, (c),(d) January, and (e),(f) February in CNTL (thin black contour) and the difference between CNTL and SMTHK (shaded). Standard deviation of the interannual variability is shown by blue contours. The 95% confidence level is shown by thick contours.

enhanced wave activity flux (Fig. 12e). Concurrently, heavy precipitation is concentrated on the eastern side of the surface cyclone (Fig. 11g). The developing structure is consistent with the composite analysis and case studies of explosive cyclones over the NWP (Yoshida and Asuma 2004; Kuwano-Yoshida and Asuma 2008; Yoshiike and Kawamura 2009).

Furthermore, the explosive deepening composite in SMTHK shows different characteristics in the upper troposphere compared with CNTL. An upper-level wave train propagating from China to the NWP appears 24 h before the explosive deepening (Fig. 12b). In contrast to the composite for the NWP events in CNTL, the positive geopotential anomaly over Japan is elongated southwestward, and the downstream negative anomaly is large. At $T = 0$ h, the positive geopotential anomaly is weaker than that in CNTL (Fig. 12d), continuing 24 h thereafter (Fig. 12f).

These results suggest that if the NWP SST front exists, the upper-level disturbance tends to couple with the surface cyclone and is associated with precipitation over the SST front, developing both the surface cyclone and the downstream upper-level ridge. In the absence of a sharp SST front, the amplification of the downstream upper-level ridge tends to be weak because the surface LHF and precipitation near the cyclone center are weak.

Figure 13 shows zonal-vertical cross sections of the temperature tendencies averaged between 30° and 45° N and from $T = -12$ to 12 h. The temperature tendency is an essential factor of the LDR diagnostic equation [Eqs. (4) and (5)]. In CNTL, the total temperature tendency $\partial T/\partial t$ between 400 and 800 hPa is larger than that in SMTHK over the cyclone, whereas it is smaller above 300 hPa (Fig. 13a). The positive temperature tendency anomaly is due to large-scale condensation (Fig. 13b). However, the temperature tendency due to dynamics

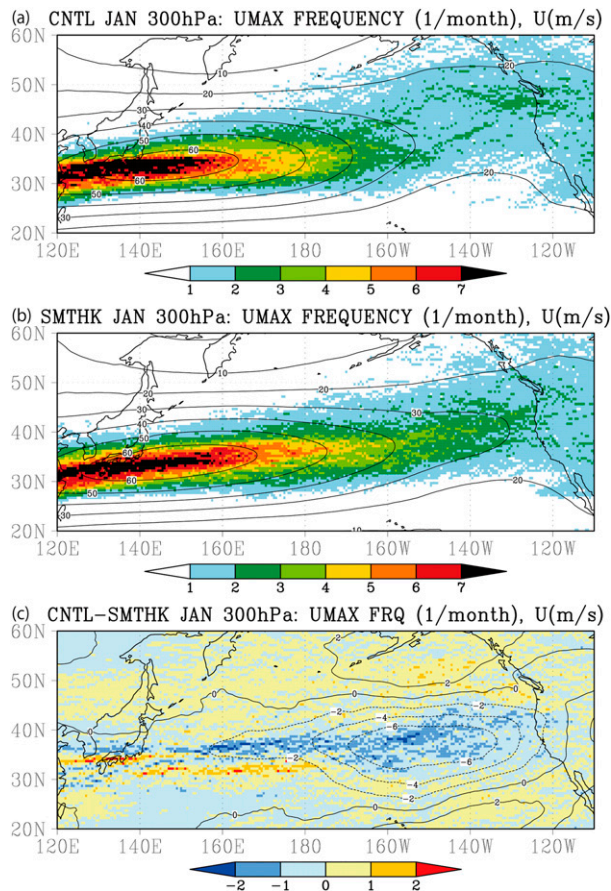


FIG. 9. Frequency of the jet axis at 300 hPa (shaded; month⁻¹) and monthly mean zonal velocity (contour; m s⁻¹) in January for (a) CNTL, (b) SMTHK, and (c) the difference between CNTL and SMTHK.

produces a negative anomaly at 300 hPa (Fig. 13c). The negative anomaly displays adiabatic cooling associated with the strong updraft induced by latent heat release, and it enhances the baroclinic structure in CNTL, which is consistent with Tamarin and Kaspi (2016). These results reveal that latent heat release associated with large-scale condensation contributes to the development in CNTL, whereas dynamical forcing in the upper-level troposphere contributes more to the development of the surface cyclone in SMTHK without concentrated precipitation.

To understand the relationship between the increase in explosive deepening events in the NWP and the SLP anomaly in the NEP found in the climatological difference between CNTL and SMTHK (Fig. 8), another composite analysis for the SLP anomaly in the NEP is conducted. The NEP SLP anomaly events in CNTL are extracted using positive 6-h SLP anomalies in CNTL relative to the climatological SLP in January in SMTHK over the region 40°–55°N, 155°–125°W. The composite is calculated by

averaging the variables when the SLP anomaly averaged over this region is positive. In contrast, the composites for negative SLP anomalies in SMTHK from the CNTL climatology in January describe the development of negative NEP SLP anomalies in SMTHK. Because the PDF of 6-h SLPs over the NEP in CNTL shows the increased frequency of high pressure events compared to SMTHK (not shown), the composites reveal the process causing the NEP SLP difference. The sample sizes are 50 in CNTL and 65 in SMTHK. The time when the sign of the SLP anomaly becomes positive (negative) from negative (positive) in CNTL (SMTHK) is defined as $T = 0$ h.

Figure 14 shows Hovmöller diagrams of the composites for the positive NEP SLP anomaly in CNTL and the negative NEP SLP anomaly in SMTHK. In CNTL, two explosive deepening events in the NWP occur from $T = -72$ to 24 h. After each event, positive geopotential anomalies develop in the NEP from $T = 0$ to 30 h (Fig. 14a). At nearly the same time, a positive SLP anomaly in the NEP and a negative precipitation anomaly along the west coast of North America develop (Fig. 14c). In contrast, the deepening rate of NWP cyclones in SMTHK is smaller than in CNTL, although the frequency is almost the same as in CNTL (Fig. 14b). A frequency of LDR24P1 of approximately once per two days in the NWP can be observed in CNTL and SMTHK as well as in the reanalysis data (not shown). After a cyclone develops in the central North Pacific in SMTHK, a negative geopotential anomaly develops over the NEP (Fig. 14b), and a positive precipitation anomaly appears along the west coast of North America, which is associated with the negative SLP anomaly in the NEP (Fig. 14d). These results suggest that the frequent development of intermittent explosive deepening events over the NWP in CNTL causes the climatological difference in the NEP SLP between CNTL and SMTHK.

The vertically integrated wave activity flux composite for the NEP SLP anomaly shows the development of the NEP SLP anomaly. The analysis shows the energy transport from the explosive cyclones to the mean SLP anomaly. When explosive deepening events occur in the NWP in CNTL, the zonal component of the wave activity flux strengthens and indicates that energy is propagating downstream (Fig. 15a). The zonal–vertical cross section averages between $T = -24$ and 120 h show that the wave activity flux develops from the lower troposphere to the upper troposphere, tilting eastward with height (Fig. 15b). Thus, the eddy activity flux associated with explosive deepening events maintains the positive SLP anomaly downstream along a Rossby wave train.

These results suggest that when the SST front exists in the NWP, strong moisture flux from the Kuroshio enhances the explosive cyclone development, and the frequent explosive deepening events cause the positive

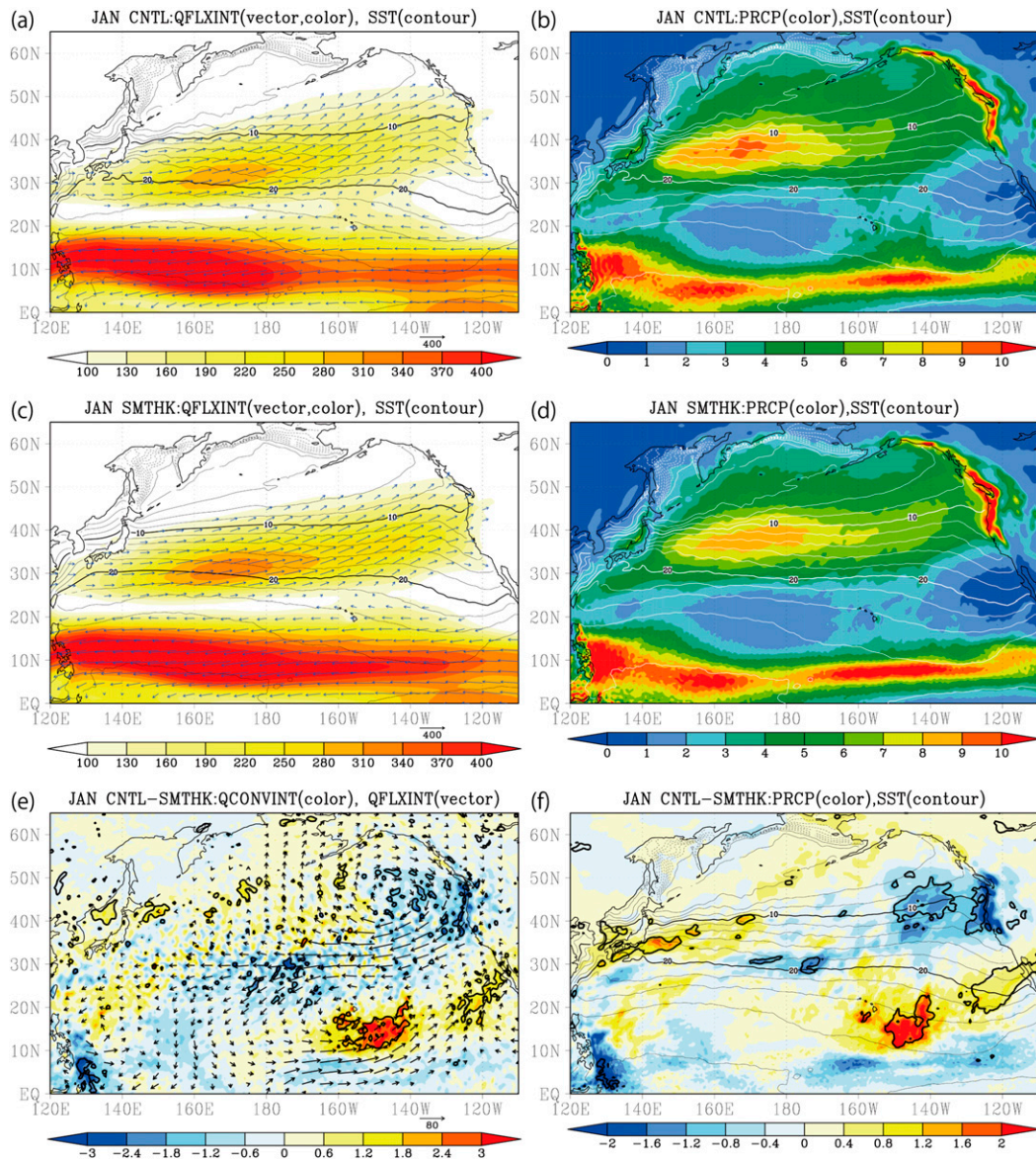


FIG. 10. Monthly average of the (left) vertically integrated horizontal moisture flux (vector; magnitude shaded, mm m s^{-1}) and (right) precipitation (shaded; mm day^{-1}) in (a),(b) CNTL, (c),(d) SMTHK, and (e),(f) the difference between CNTL and SMTHK in January; the 95% confidence level is also shown (thick contour). The SST in CNTL is shown by thin contours ($^{\circ}\text{C}$; CI: 2°C).

SLP anomaly in the NEP through the downstream energy flux from the cyclone development. Once the positive SLP anomaly develops in the NEP, it inhibits cyclone development in the NEP. In the smoothed SST front, moisture contributing to cyclone development must be gathered from a broader area, and coupling between the upper-level trough and the surface cyclone is weakened, causing a reduction in explosive deepening events in the NWP. As a result, explosive deepening events increase in the central North Pacific, causing the cyclonic SLP anomaly in the NEP. The cyclonic

anomaly works to maintain the zonal jet. These responses to the SST front in CNTL and SMTHK produce the differences in the climatological SLP, jet meandering, and precipitation between the two experiments.

TABLE 1. Sampling size of explosive and slow deepening events in the NWP.

CNTL		SMTHK	
Explosive	Slow	Explosive	Slow
93	501	83	560

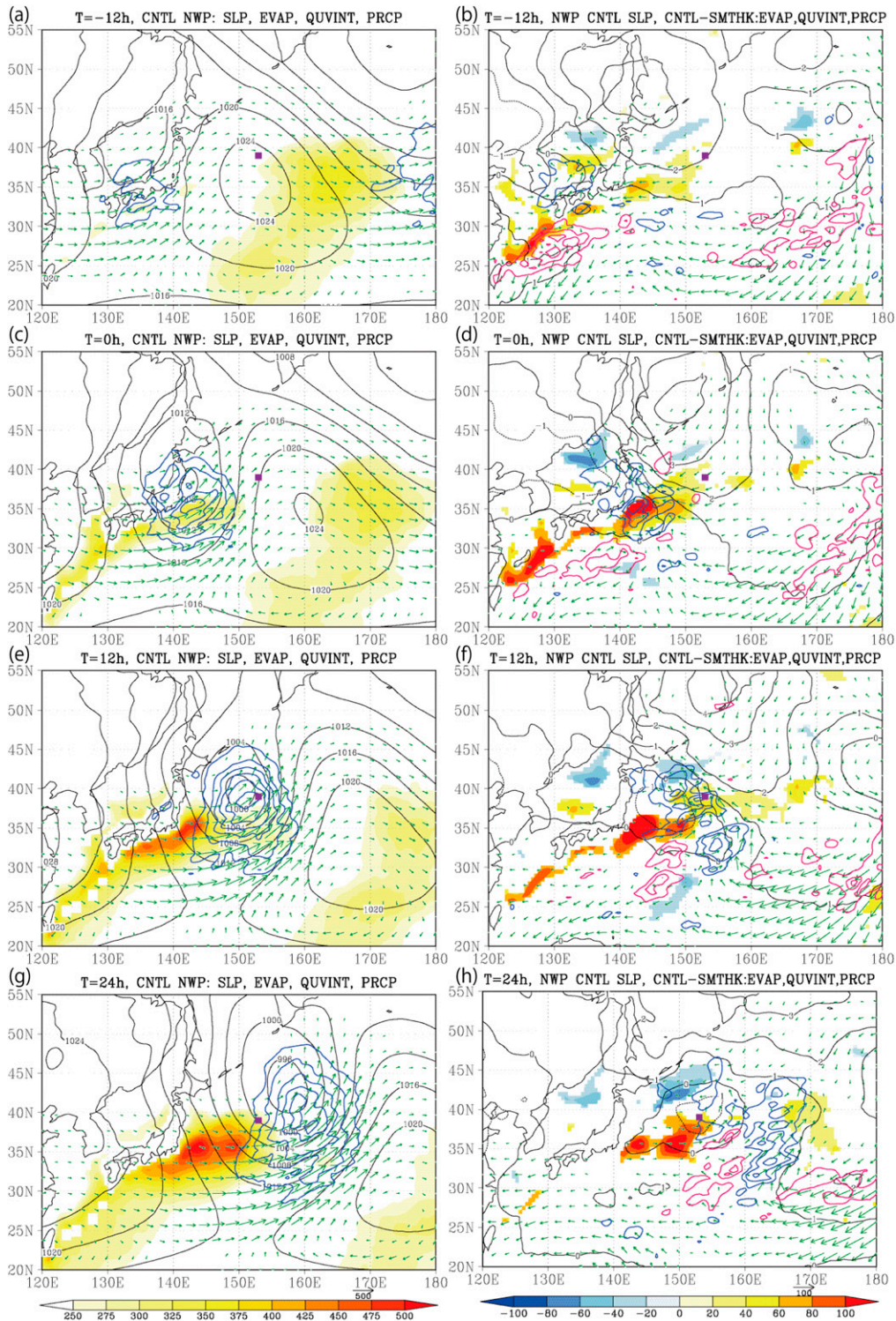


FIG. 11. The composites of explosive deepening events in the NWP (magenta square at $T = 0$ h) for (left) CNTL and (right) CNTL – SMTHK at $T =$ (a),(b) –12, (c),(d) 0, (e),(f) 12, and (g),(h) 24 h; SLP (black contour; hPa), surface latent heat flux (shaded; W m^{-2}), vertically integrated moisture flux (green vector; mm s^{-1}), and precipitation [blue contour in CNTL with CI of 5 mm day^{-1} from 10 mm day^{-1} ; blue (positive) and purple (negative) contours in CNTL – SMTHK with CI of 3 mm day^{-1} without zero contours] are shown.

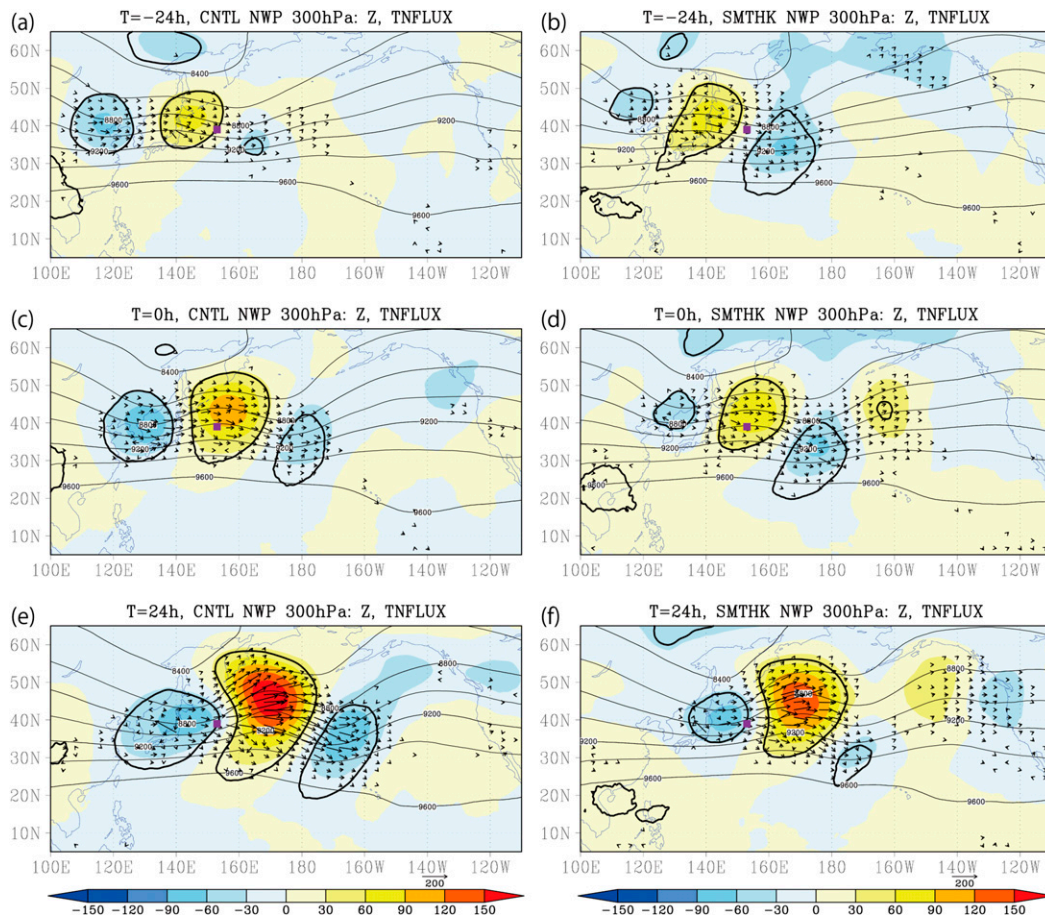


FIG. 12. (left) CNTL and (right) SMTHK composites of explosive deepening events at 39°N , 153°E (magenta square); the geopotential height at 300 hPa (thin contour; m) and the difference from the composite of slow deepening events (shaded; m) and the eddy activity flux (vector; $\text{m}^2 \text{s}^{-2}$) at $T =$ (a),(b) -24 , (c),(d) 0 , and (e),(f) 24 h are shown. Thick contours show the 95% confidence levels of the geopotential height anomalies.

Given that the EGR and eddy components of meridional heat transport show only weak responses over the NWP SST front in the experiments (Figs. 4 and 5), the increase in explosive deepening events associated with the SST front in the NWP can cause the large-scale response without the change in the mean meridional heat transport due to the eddy component. The atmospheric response to the SST front through explosive cyclone development is a new mechanism and contributes to the argument of the remote response to the NWP SST front.

6. Intraseasonal dependency

In the present study, the organized LDR24P1 difference appears only in January, not in December and February (Fig. 2). Although this intraseasonal dependency is consistent with that reported by Taguchi et al. (2012), Smirnov et al. (2015) showed that the atmospheric response is

significant throughout winter in their numerical experiments. To understand the intraseasonal dependency in the present study, upper-level disturbance activity and moisture flux, which work as essential factors for explosive deepening (Shapiro et al. 1999; Yoshida and Asuma 2004), in December and February are compared with those in January. The SST differences between CNTL and SMTHK are similar among the three months (not shown).

Figure 16 shows the monthly climatology differences between two successive months (December minus January and February minus January) for $v'u'$, the surface LHF, the vertically integrated horizontal moisture flux, and precipitable water along with their January values. The monthly means are combined averages of the CNTL and SMTHK experiments (ALL). In December, $v'u'$ is enhanced to the north of the January maximum around 40°N from the surface to 250 hPa (Figs. 16a,c). The maximum $v'u'$ at 850 hPa in December is located along 45°N (not shown), which is shifted northward by

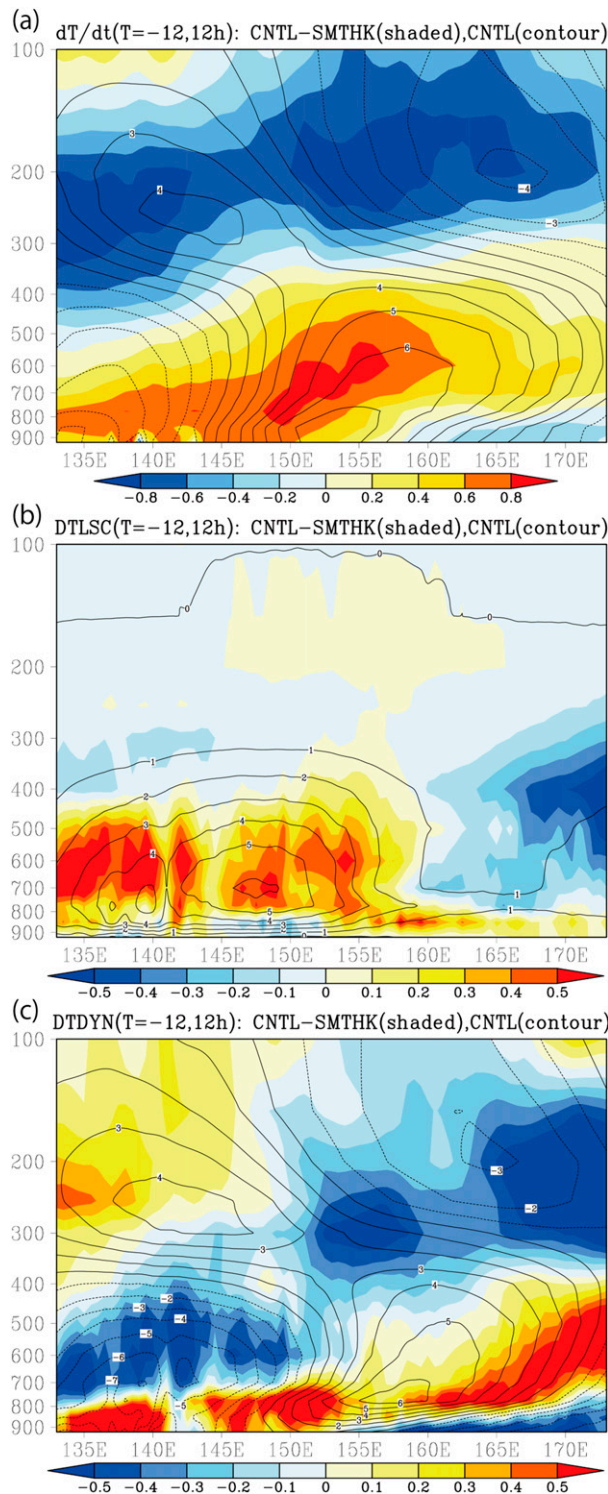


FIG. 13. Zonal-vertical cross sections of the composites for explosive deepening events in the NWP (39°N , 153°E) in CNTL (contour) and CNTL – SMTHK (shaded) for the (a) temperature tendency $\partial T/\partial t$, (b) large-scale condensation, and (c) dynamics averaged between 30° and 45°N from $T = -12$ to 12 h (K day^{-1}).

10° relative to that in January. Moreover, $v'v'$ at 850 hPa over the East China Sea is weaker than in January (Fig. 16c). The LHF from the Kuroshio along the southern coast of Japan is somewhat smaller in December than in January (Fig. 16e), whereas moisture from the subtropics over the NWP is greater in December than in January (Fig. 16g). The situation suggests that in December, the climatological storm track associated with the upper-level disturbance is far from the SST front, and the large moisture flux from the subtropics suppresses the evaporation response to the SST front, resulting in a weak response in explosive deepening to the SST front and the warm SST anomaly.

In February, the magnitude of the upper-level disturbances shown by $v'v'$ is stronger than in January; the latitude of the maximum does not change (Fig. 16b), and $v'v'$ in the lower troposphere is also active near the SST front (Fig. 16d). However, the surface LHF is much smaller in February than in January over the NWP, including the Kuroshio and its extension (Fig. 16f). Instead, the horizontal moisture flux is strong in the Kuroshio region, extending from southeastern China and the subtropics (Fig. 16h). These results suggest that weak surface evaporation restricts the explosive deepening response to the SST front. In this situation, the strong upper-level disturbances can be a dominant factor for explosive cyclone deepening relative to surface evaporation along the SST front in February. Indeed, the contribution of LSC in Eq. (5) to the explosive deepening in February is smaller than in January (not shown). The small evaporation is due to cold air with low saturated specific humidity in February. Nakamura (1992) discussed that the lower specific humidity in the midwinter relative to spring and autumn may be one of the factors of the “midwinter suppression” of baroclinic wave activity in the Pacific, which occurs from January to February in observations. Consequently, the atmospheric response to the SST front depends on the atmospheric temperature and moisture amount around the SST front and the relative location of the upper-level jet.

7. Conclusions

To understand atmospheric responses to the NWP SST fronts, parallel 20-yr integrations of an AGCM with 50-km horizontal resolution are conducted with observed daily SSTs (CNTL) and smoothed SSTs (SMTHK) over the NWP. The results show the significant response of explosive deepening events in extratropical cyclones and large-scale circulation over the North Pacific in January. In CNTL, explosive deepening events increase

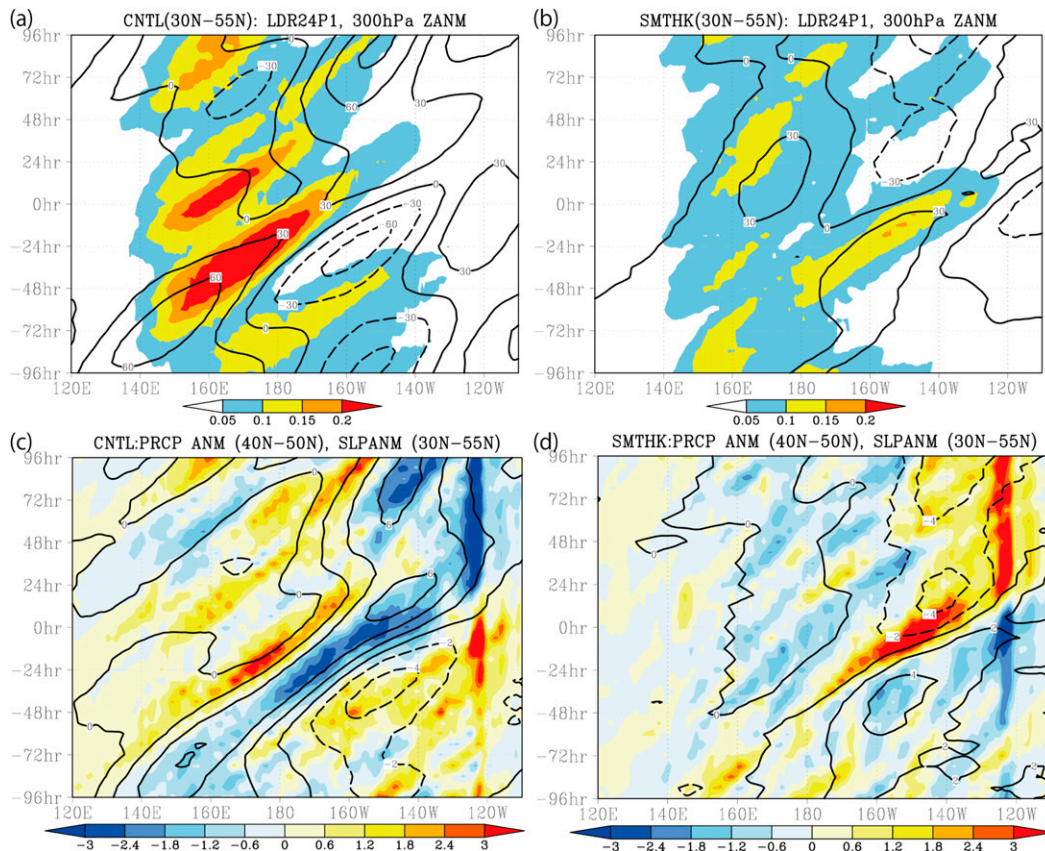


FIG. 14. (left) Time (vertical axis) and longitude (horizontal axis) composites for the positive SLP anomalies over the NEP in CNTL from the January climatology in SMTHK and (right) for the negative SLP anomalies over the NEP in SMTHK from the January climatology in CNTL; (a),(b) LDR24P1 (shaded; hPa day^{-1}) and geopotential height anomaly at 300 hPa averaged between 30° and 55°N (m; contour; solid line is positive, and broken line is negative) and (c),(d) precipitation anomaly averaged between 40° and 50°N (shaded; mm day^{-1}).

(decrease) over the NWP (NEP) compared to SMTHK. The increase is due to the diabatic heating by large-scale condensation, which is enhanced by the anomalous surface evaporation from the Kuroshio and its extension. The EGR diagnostic suggests that dry dynamics are not significantly different between the two experiments because the static stability response counteracts the vertical shear response. In CNTL compared with SMTHK, there is a large static stability response over the cold side of the SST front due to the meridionally asymmetric SST and surface heat flux anomalies and cold air advection associated with the high pressure anomaly over the Okhotsk Sea.

The large-scale responses occur over the NEP. The barotropic geopotential height response over the Gulf of Alaska is accompanied by the meridional spread in the occurrence frequency of the upper-level westerly jet axis and precipitation distribution along the west coast of North America and southeast of Hawaii. The composite of the NEP SLP anomaly shows that frequent explosive cyclonic development over the NWP brings the high

pressure anomaly in the NEP, together with the precipitation anomaly in the subtropics in CNTL. The composite analyses for SMTHK demonstrate that weaker explosive cyclones in the NWP result in the negative height anomaly in the Gulf of Alaska and precipitation increase along the west coast of North America and decrease southeast of Hawaii. The asymmetric response is consistent with O'Reilly and Czaja (2015), who reported that the stronger SST front associated with the Kuroshio Extension enhances the storm track in the NWP, whereas the storm track spreads zonally under a weaker SST front based on observed SST and reanalysis data. Furthermore, the large-scale response pattern is quite similar to the results of recent sensitivity experiments using AGCMs (Smirnov et al. 2015; Zhou et al. 2015) and a regional model (Ma et al. 2015). Especially, the diabatic heating structure associated with a synoptic baroclinic wave in Ma et al. (2015) is quite similar to the present study, whereas the high-resolution experiment in Smirnov et al. (2015) showed

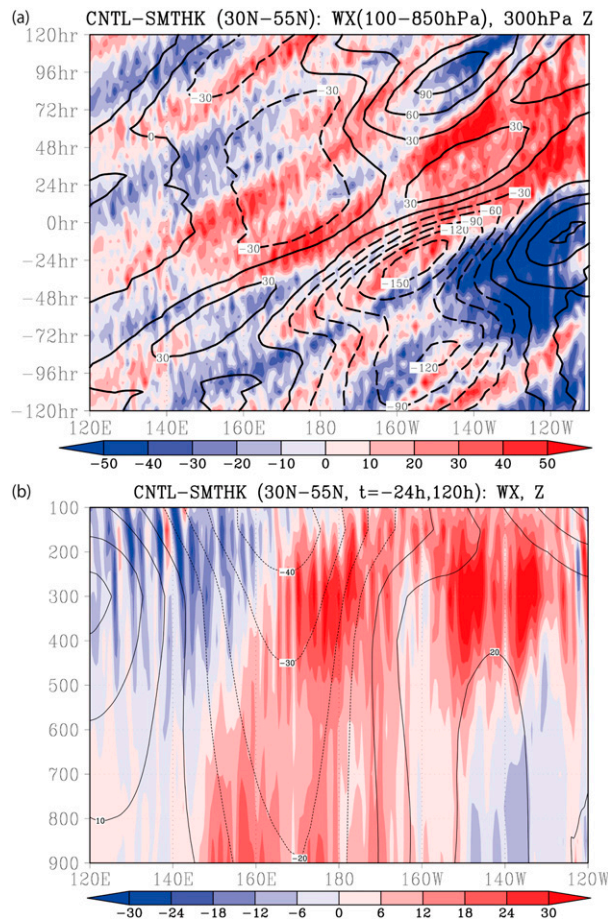


FIG. 15. Composites of wave activity flux (shaded; $m^2 s^{-2}$) and geopotential height (contour; m) for the NEP SLP anomalies in (a) time (vertical axis) and longitude (horizontal axis) slices for the CNTL – SMTHK differences in the wave activity flux zonal component vertically averaged from 100 to 850 hPa and the 300-hPa geopotential height. (b) Vertical–zonal cross section of the CNTL – SMTHK differences in the wave activity flux zonal component and geopotential height averaged between 30° and $55^\circ N$ and between $T = -24$ and 120 h.

significant responses in $v'T'$ at 850 hPa and precipitation, which differ in the present study. Their studies and the present work commonly use 25- to 50-km horizontal resolutions, which allow the oceanic frontal- and eddy-scale SST distribution to be resolved, even though the SST anomalies are considerably different between the studies. Numerical models with such a high horizontal resolution can cause a strong precipitation response to SST anomalies, as shown in Ma et al. (2015) and Smirnov et al. (2015), and the precipitation response could result in explosive cyclone development, as demonstrated in the present study. Atmospheric models of these resolutions will be used in the High Resolution Model Intercomparison Project (HighResMIP; Haarsma et al. 2016) as a part of

CMIP6 and will contribute to understanding the atmospheric response to SST fronts.

In addition to the horizontal resolution, the sample size is an important factor to consider when examining the importance of SST fronts relative to internally generated variability. Indeed, the 20-yr integration in the present study is too short to remove the interannual variation of the Aleutian low (Fig. 8); thus, it is possible that statistically significant responses can be found in the region of strong interannual variability with longer integration. In the context of MIPs, the internal variability may be different between models and should be carefully analyzed along with different means between models.

The results of the sensitivity experiment suggest that the SST anomalies associated with the western boundary currents in the NWP can anchor the upper-level disturbance propagating from upstream and increase explosive deepening events through diabatic heating, even if the SST front effect is weaker than that over the Gulf Stream (Iizuka et al. 2013; Small et al. 2014). Frequent cyclone development enhances upper-level jet meandering and inhibits storm activity in the NEP. In the smoothed SST front, the upper-level disturbances pass relatively unchanged over the NWP, causing explosive cyclogenesis in the central North Pacific and the NEP and a more zonal upper-level jet.

The present results suggest that SST biases associated with the NWP SST front in major climate models used for climate change projection and seasonal prediction may affect the behavior of the storm track and Aleutian low in the models in addition to local precipitation, as reported by Long and Xie (2015). For example, Fig. 17 shows the climatological SST difference in January between observations and a historical run of MIROC4h (Sakamoto et al. 2012), which is one of the highest-resolution models in CMIP5, with a spectral T213 resolution for the atmospheric component and 0.28125° (zonal) and 0.1875° (meridional) horizontal resolutions in the ocean. The SST difference shows a warm anomaly along the Oyashio front, and the SST bias is comparable with the SST difference between CNTL and SMTHK (Fig. 1). Given that the horizontal resolution of the atmospheric component in MIROC4h is almost the same as that of the AGCM used in the present study, the storm track and large-scale circulation in the North Pacific in MIROC4h can deviate from the observed atmospheric circulation owing to the SST bias.

A comparison between LDR and EGR analyses suggests that the horizontal distribution of the modeled SST anomaly can cause different atmospheric responses to SST fronts. For example, the AGCM experiments using observed and smoothed SSTs over the Gulf Stream by Small et al. (2014) showed substantial changes in $v'T'$ in the lower troposphere in contrast to

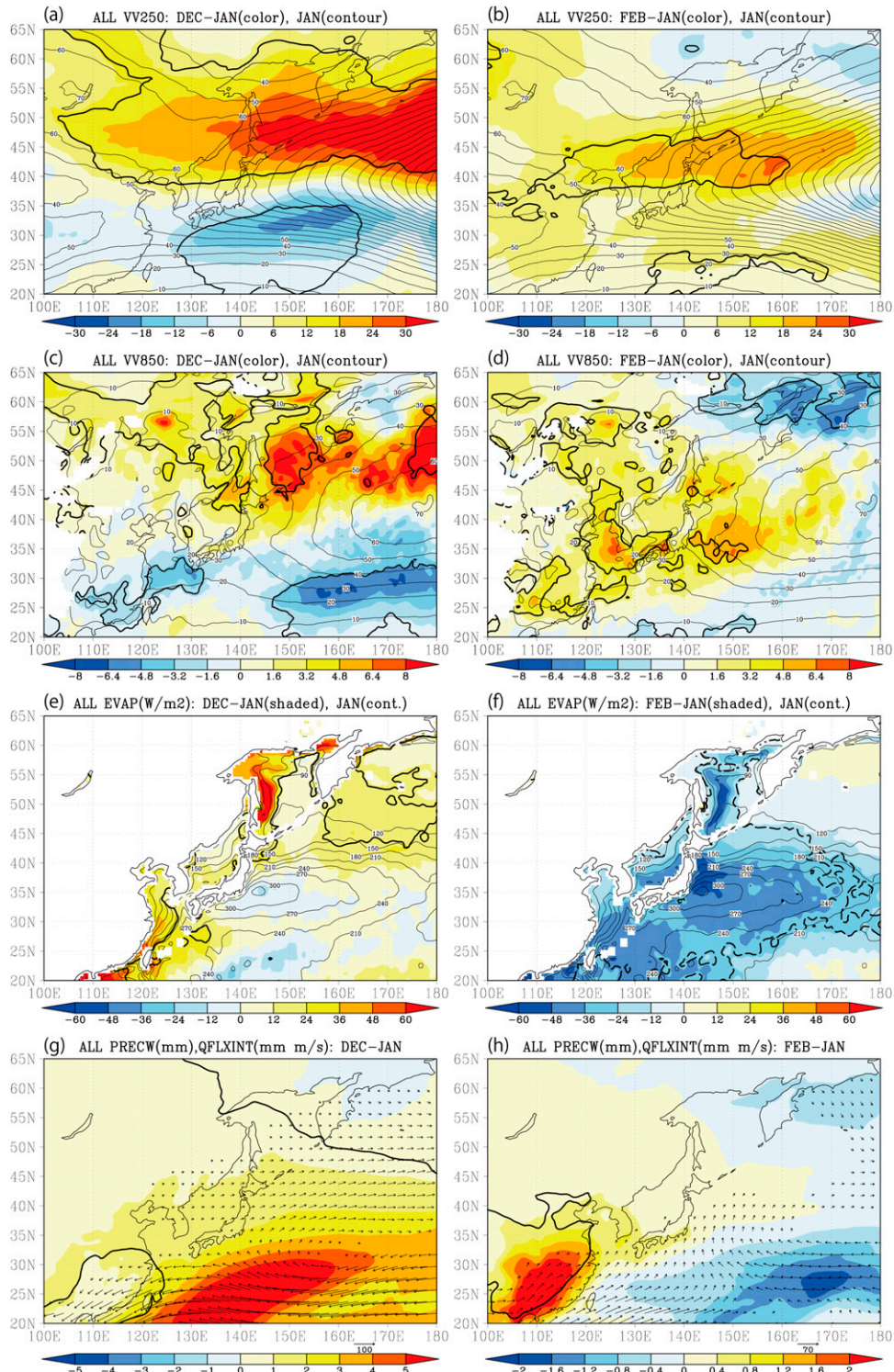


FIG. 16. Combined monthly climatology using CNTL and SMTHK (ALL) (thin contour) and the difference from that in January (shaded) in (left) December and (right) February; $v'v'$ at (a),(b) 250 hPa ($\text{m}^2 \text{s}^{-2}$) and (c),(d) 850 hPa, and (e),(f) surface latent heat flux (W m^{-2}). (g),(h) The differences from January in terms of the precipitable water (shaded; mm) and vertically integrated moisture flux (vector; mm m s^{-1}) are shown. The 95% confidence levels for shaded variables are shown by thick contours.

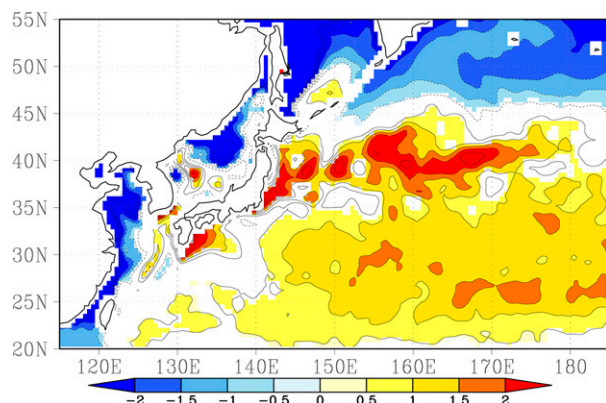


FIG. 17. SST difference (K) in January averaged from 1982 to 2001 between CNTL and MIROC4h.

small changes in the heat flux found in the present study. Small et al.'s (2014, their Fig. 14) EGR change at 850 hPa was positive over the front and was sandwiched by negative changes on either side, which is qualitatively similar to our result, although their positive change was much larger than the negative ones, which contradicts the weak positive EGR change in our model. The different EGR changes in Small et al.'s (2014) simulations and our study may be partly due to different SST anomalies to the north and south of the front. The SST anomaly to the south of the front was stronger than that to the north in their experiments, although the opposite is true in our experiments. Because the SST anomalies north of the front induce a stabilizing effect on the EGR and counteract the shear effect, as described in section 3, the stability effect would be weak in Small et al. (2014), probably resulting in a large EGR change. To cancel the stability and shear effects on the EGR, dipole SST anomalies with substantial amplitudes in the northern pole are necessary. Indeed, the SST anomaly analyzed in Smirnov et al. (2015) and Taguchi et al. (2012) in the NWP was characterized by a monopole structure and tended to show significant EGR responses in the lower troposphere along the SST fronts. Multimodel experiments with the same SST anomaly contribute to better understanding the atmospheric response to the midlatitude SST front.

The month-to-month difference in the present experiment suggests that intraseasonal differences in the atmospheric response between numerical model experiments may be affected by the relationship between upper-level disturbances and surface evaporation. The atmospheric response to the SST anomaly becomes significant in the present experiment only when the upper-level disturbances pass over the surface evaporation

anomaly and the surface evaporation is sufficiently large to influence the explosive deepening.

To conclude, the present study reveals that the LHF from the Kuroshio and its extension enhance explosive cyclones and cause local- and basin-scale atmospheric responses to the SST front. The present results suggest that the coupling between explosive cyclones and SST fronts is important for the climate state and variability as well as numerical weather prediction, as demonstrated by Hirata et al. (2015). Although some recent studies have shown that model biases and uncertainties related to explosive cyclones and the storm track in CMIP models are passively affected by the large-scale environment (Nishii et al. 2015; Harvey et al. 2015; Seiler and Zwiers 2016), the present study suggests that the explosive cyclone biases can be a result of the interaction between explosive cyclones and the large-scale environment. In addition, the storm-track response to the SST anomalies is sensitive to the horizontal resolution of atmospheric models (Willison et al. 2013, 2015; Smirnov et al. 2015). Therefore, multiresolution experiments with coordinated SST anomalies using multi-AGCMs and atmosphere–ocean coupled GCMs will contribute to better understanding the interaction among SST fronts, the storm track, and large-scale circulations in the climate system.

Acknowledgments. We thank Akira Yamazaki for calculating the eddy components. This research was supported by the Japan Society for the Promotion of Science (JSPS) KAKENHI Grants 25242038, 26707025, 26287110, 15H01606, 16K12591, and 16H01846 as well as the Grant-in-Aid for Scientific Research on Innovative Areas 22106008 (“A ‘hot spot’ in the climate system: Extra-tropical air–sea interaction under the East Asian monsoon system”) from the Ministry of Education, Culture, Sports, Science, and Technology of Japan. The AFES was calculated using the Earth Simulator under JAMSTEC support.

REFERENCES

- Booth, J. F., L. Thompson, J. Patoux, and K. A. Kelly, 2012: Sensitivity of midlatitude storm intensification to perturbations in the sea surface temperature near the Gulf Stream. *Mon. Wea. Rev.*, **140**, 1241–1256, doi:10.1175/MWR-D-11-00195.1.
- Enomoto, T., A. Kuwano-Yoshida, N. Komori, and W. Ohfuchi, 2008: Description of AFES 2: Improvements for high-resolution and coupled simulations. *High Resolution Numerical Modelling of the Atmosphere and Ocean*, H. Kevin and O. Wataru, Eds., Springer, 77–97.
- Fink, A., S. Pohle, J. Pinto, and P. Knippertz, 2012: Diagnosing the influence of diabatic processes on the explosive deepening of extratropical cyclones. *Geophys. Res. Lett.*, **39**, L07803, doi:10.1029/2012GL051025.

- Frankignoul, C., N. Sennéchal, Y.-O. Kwon, and M. A. Alexander, 2011: Influence of the meridional shifts of the Kuroshio and the Oyashio Extensions on the atmospheric circulation. *J. Climate*, **24**, 762–777, doi:10.1175/2010JCLI3731.1.
- Haarsma, R. J., and Coauthors, 2016: High Resolution Model Intercomparison Project (HighResMIP). *Geosci. Model Dev.*, **9**, 4185–4208, doi:10.5194/gmd-9-4185-2016.
- Harvey, B. J., L. C. Shaffrey, and T. J. Woollings, 2015: Deconstructing the climate change response of the Northern Hemisphere wintertime storm tracks. *Climate Dyn.*, **45**, 2847–2860, doi:10.1007/s00382-015-2510-8.
- Hirata, H., R. Kawamura, M. Kato, and T. Shinoda, 2015: Influential role of moisture supply from the Kuroshio/Kuroshio Extension in the rapid development of an extratropical cyclone. *Mon. Wea. Rev.*, **143**, 4126–4144, doi:10.1175/MWR-D-15-0016.1.
- Hotta, D., and H. Nakamura, 2011: On the significance of the sensible heat supply from the ocean in the maintenance of the mean baroclinicity along storm tracks. *J. Climate*, **24**, 3377–3401, doi:10.1175/2010JCLI3910.1.
- Iizuka, S., M. Shiota, R. Kawamura, and H. Hatsushika, 2013: Influence of the monsoon variability and sea surface temperature front on the explosive cyclone activity in the vicinity of Japan during northern winter. *SOLA*, **9**, 1–4, doi:10.2151/sola.2013-001.
- Kuwano-Yoshida, A., 2014: Using the local deepening rate to indicate extratropical cyclone activity. *SOLA*, **10**, 199–203, doi:10.2151/sola.2014-042.
- , and Y. Asuma, 2008: Numerical study of explosively developing extratropical cyclones in the northwestern Pacific region. *Mon. Wea. Rev.*, **136**, 712–740, doi:10.1175/2007MWR2111.1.
- , T. Enomoto, and W. Ohfuchi, 2010a: An improved PDF cloud scheme for climate simulations. *Quart. J. Roy. Meteor. Soc.*, **136**, 1583–1597, doi:10.1002/qj.660.
- , S. Minobe, and S.-P. Xie, 2010b: Precipitation response to the Gulf Stream in an atmospheric GCM. *J. Climate*, **23**, 3676–3698, doi:10.1175/2010JCLI3261.1.
- , B. Taguchi, and S.-P. Xie, 2013: Baiu rainband termination in atmospheric and coupled atmosphere–ocean models. *J. Climate*, **26**, 10 111–10 124, doi:10.1175/JCLI-D-13-00231.1.
- Lindzen, R. S., and B. Farrell, 1980: A simple approximate result for the maximum growth rate of baroclinic instabilities. *J. Atmos. Sci.*, **37**, 1648–1654, doi:10.1175/1520-0469(1980)037<1648:ASARFT>2.0.CO;2.
- Long, S., and S. Xie, 2015: Intermodel variations in projected precipitation change over the North Atlantic: Sea surface temperature effect. *Geophys. Res. Lett.*, **42**, 4158–4165, doi:10.1002/2015GL063852.
- Ma, X., and Coauthors, 2015: Distant influence of Kuroshio eddies on North Pacific weather patterns? *Sci. Rep.*, **5**, 17785, doi:10.1038/srep17785.
- Minobe, S., A. Kuwano-Yoshida, N. Komori, S.-P. Xie, and R. J. Small, 2008: Influence of the Gulf Stream on the troposphere. *Nature*, **452**, 206–209, doi:10.1038/nature06690.
- Nakamura, H., 1992: Midwinter suppression of baroclinic wave activity in the Pacific. *J. Atmos. Sci.*, **49**, 1629–1642, doi:10.1175/1520-0469(1992)049<1629:MSOBWA>2.0.CO;2.
- , T. Sampe, Y. Tanimoto, and A. Shimpo, 2004: Observed associations among storm tracks, jet streams and midlatitude oceanic fronts. *Earth's Climate: The Ocean–Atmosphere Interaction*, *Geophys. Monogr.*, Vol. 147, Amer. Geophys. Union, 329–345.
- Nakamura, M., and S. Yamane, 2010: Dominant anomaly patterns in the near-surface baroclinicity and accompanying anomalies in the atmosphere and oceans. Part II: North Pacific basin. *J. Climate*, **23**, 6445–6467, doi:10.1175/2010JCLI3017.1.
- Nishii, K., H. Nakamura, and Y. J. Orsolini, 2015: Arctic summer storm track in CMIP3/5 climate models. *Climate Dyn.*, **44**, 1311–1327, doi:10.1007/s00382-014-2229-y.
- Ogawa, F., H. Nakamura, K. Nishii, T. Miyasaka, and A. Kuwano-Yoshida, 2012: Dependence of the climatological axial latitudes of the tropospheric westerlies and storm tracks on the latitude of an extratropical oceanic front. *Geophys. Res. Lett.*, **39**, L05804, doi:10.1029/2011GL049922.
- Ohfuchi, W., and Coauthors, 2004: 10-km mesh meso-scale resolving simulations of the global atmosphere on the Earth Simulator—preliminary outcomes of AFES (AGCM for the Earth Simulator). *J. Earth Simul.*, **1**, 8–34.
- Onogi, K., and Coauthors, 2007: The JRA-25 Reanalysis. *J. Meteor. Soc. Japan*, **85**, 369–432, doi:10.2151/jmsj.85.369.
- O'Reilly, C. H., and A. Czaja, 2015: The response of the Pacific storm track and atmospheric circulation to Kuroshio Extension variability. *Quart. J. Roy. Meteor. Soc.*, **141**, 52–66, doi:10.1002/qj.2334.
- , S. Minobe, and A. Kuwano-Yoshida, 2016: The influence of the Gulf Stream on wintertime European blocking. *Climate Dyn.*, **47**, 1545–1567, doi:10.1007/s00382-015-2919-0.
- Parfitt, R., A. Czaja, S. Minobe, and A. Kuwano-Yoshida, 2016: The atmospheric frontal response to SST perturbations in the Gulf Stream region. *Geophys. Res. Lett.*, **43**, 2299–2306, doi:10.1002/2016GL067723.
- Reynolds, R. W., T. M. Smith, C. Liu, D. B. Chelton, K. S. Casey, and M. G. Schlax, 2007: Daily high-resolution-blended analyses for sea surface temperature. *J. Climate*, **20**, 5473–5496, doi:10.1175/2007JCLI1824.1.
- Sakamoto, T. T., and Coauthors, 2012: MIROC4h—a new high-resolution atmosphere–ocean coupled general circulation model. *J. Meteor. Soc. Japan*, **90**, 325–359, doi:10.2151/jmsj.2012-301.
- Sampe, T., H. Nakamura, A. Goto, and W. Ohfuchi, 2010: Significance of a midlatitude SST frontal zone in the formation of a storm track and an eddy-driven westerly jet. *J. Climate*, **23**, 1793–1814, doi:10.1175/2009JCLI3163.1.
- Sanders, F., and J. Gyakum, 1980: Synoptic-dynamic climatology of the “bomb.” *Mon. Wea. Rev.*, **108**, 1589–1606, doi:10.1175/1520-0493(1980)108<1589:SDCOT>2.0.CO;2.
- Seiler, C., and F. W. Zwiers, 2016: How well do CMIP5 climate models reproduce explosive cyclones in the extratropics of the Northern Hemisphere? *Climate Dyn.*, **46**, 1241–1256, doi:10.1007/s00382-015-2642-x.
- Shapiro, M., and Coauthors, 1999: A planetary-scale to mesoscale perspective of the life cycles of extratropical cyclones: The bridge between theory and observations. *The Life Cycles of Extratropical Cyclones*, M. Shapiro and S. Gronas, Eds., Amer. Meteor. Soc., 139–186.
- Small, R. J., R. A. Tomas, and F. O. Bryan, 2014: Storm track response to ocean fronts in a global high-resolution climate model. *Climate Dyn.*, **43**, 805–828, doi:10.1007/s00382-013-1980-9.
- Smirnov, D., M. Newman, M. A. Alexander, Y.-O. Kwon, and C. Frankignoul, 2015: Investigating the local atmospheric response to a realistic shift in the Oyashio sea surface temperature front. *J. Climate*, **28**, 1126–1147, doi:10.1175/JCLI-D-14-00285.1.
- Taguchi, B., H. Nakamura, M. Nonaka, and S. P. Xie, 2009: Influences of the Kuroshio/Oyashio Extensions on air–sea heat exchanges and storm-track activity as revealed in regional atmospheric model simulations for the 2003/04 cold season. *J. Climate*, **22**, 6536–6560, doi:10.1175/2009JCLI2910.1.

- , —, —, N. Komori, A. Kuwano-Yoshida, K. Takaya, and A. Goto, 2012: Seasonal evolutions of atmospheric response to decadal SST anomalies in the North Pacific subarctic frontal zone: Observations and a coupled model simulation. *J. Climate*, **25**, 111–139, doi:10.1175/JCLI-D-11-00046.1.
- Takaya, K., and H. Nakamura, 1997: A formulation of a wave-activity flux for stationary Rossby waves on a zonally varying basic flow. *Geophys. Res. Lett.*, **24**, 2985–2988, doi:10.1029/97GL03094.
- Tamarin, T., and Y. Kaspi, 2016: The poleward motion of extratropical cyclones from a potential vorticity tendency analysis. *J. Atmos. Sci.*, **73**, 1687–1707, doi:10.1175/JAS-D-15-0168.1.
- Willison, J., W. A. Robinson, and G. M. Lackmann, 2013: The importance of resolving mesoscale latent heating in the North Atlantic storm track. *J. Atmos. Sci.*, **70**, 2234–2250, doi:10.1175/JAS-D-12-0226.1.
- , —, and —, 2015: North Atlantic storm-track sensitivity to warming increases with model resolution. *J. Climate*, **28**, 4513–4524, doi:10.1175/JCLI-D-14-00715.1.
- Woollings, T., B. Hoskins, M. Blackburn, D. Hassell, and K. Hodges, 2010: Storm track sensitivity to sea surface temperature resolution in a regional atmosphere model. *Climate Dyn.*, **35**, 341–353, doi:10.1007/s00382-009-0554-3.
- Yin, J. H., 2005: A consistent poleward shift of the storm tracks in simulations of 21st century climate. *Geophys. Res. Lett.*, **32**, L18701, doi:10.1029/2005GL023684.
- Yoshida, A., and Y. Asuma, 2004: Structures and environment of explosively developing extratropical cyclones in the north-western Pacific region. *Mon. Wea. Rev.*, **132**, 1121–1142, doi:10.1175/1520-0493(2004)132<1121:SAEOED>2.0.CO;2.
- Yoshiike, S., and R. Kawamura, 2009: Influence of wintertime large-scale circulation on the explosively developing cyclones over the western North Pacific and their downstream effects. *J. Geophys. Res.*, **114**, D13110, doi:10.1029/2009JD011820.
- Zhou, G., M. Latif, R. J. Greatbatch, and W. Park, 2015: Atmospheric response to the North Pacific enabled by daily sea surface temperature variability. *Geophys. Res. Lett.*, **42**, 7732–7739, doi:10.1002/2015GL065356.